Optical sensors for acoustic detection

Lucas Borges da Silva

A thesis submitted in partial satisfaction of the requirements for the degree of Master in Physics Engineering

Supervisor: Prof. Orlando Frazão

co-Supervisor: Prof. José Luís dos Santos

Department of Physics and Astronomy

Faculty of Sciences of the University of Porto

October 2014

Acknowledgments

First I would like to thank Prof. Orlando Frazão for his support and expertise throughout this journey. His immense experience and practical knowledge were a source of invaluable advice. To him I am very grateful.

I would also like to thank Prof. José Luís dos Santos for his kindness and sincere comprehension. It allowed me to conciliate my work with the pursuit of my own dreams outside the academic life, something I am truly thankful for.

To all the INESC staff and researchers I would like to leave a kind word of gratefulness for the warm welcome and the ever present will to help in spite of the long and annoying hours of buzzing piezoelectrics. A special acknowledgement to Hugo Martins whose aid was indispensable for the development of this thesis.

To all the staff and researchers at the University of Manchester Aerospace Research Institute I would like to express my gratitude for the sympathy and kindness with which I was welcomed and treated throughout my staying in the UK. To Dr. Clara Frias a special note of gratitude for the opportunity to work in such high-standard facilities. Her professionalism and guidance were a great example for me. I would also like to thank Mohamed Saleh and Shankhachur Roy for the companionship and shared knowledge.

To my friends, whose words of motivation never ceased to spring throughout all these years, a big thank you. In between light cafe conversations and lunch time philosophical shared thoughts I've learnt a great deal from you all.

To my family, whose unconditional support has led me here, I am forever grateful. Without your support and comprehension I would never have made it this far.

Lastly I am deeply thankful to Inês, for her unassailable support and tenderness, for loving and caring regardless of everything. Thank you for giving me strength when none seemed to be found. Thank you for being a part of my life.

Abstract

In the last few decades optical fibre sensors emerged as a great promise as sensing devices. High sensitivity coupled with small-size features and remarkable shielding properties in demanding environments motivate the gradual replacement of the conventional electric-based setups. In particular, their development in the branch of acoustic sensing came to help suppress the need for a more stable and reliable method to monitor large scale structures and measure challenging surroundings.

Concerning the marked necessity for fibre optic sensors to establish themselves as trustworthy designs with improved performance over the traditional piezoelectrics, this dissertation provides a study of two major optical fibre sensor configurations. Fabry-Pérot interferometers and fibre Bragg gratings were developed for the detection of acoustic waves and had their performances compared. Several sensing heads were characterized with the aid of a piezoelectric acting as an acoustic source. The results emphasize the prospects of micro-applications for Fabry-Pérot sensors and enhance the qualities of FBGs as very sensitive and flexible devices capable of multiplexing. The ability to detect acoustic emissions that are typical from aging processes makes these sensors suitable for structural health monitoring.

Keywords: Fibre optic sensors; acoustic sensing; Fabry-Pérot; fibre Bragg gratings.

Resumo

Nas últimas décadas os sensores em fibra ótica têm emergido como soluções muito promissoras na área dos dispositivos sensores. Alta sensibilidade associada às suas características próprias de pequenas escalas e propriedades notáveis de blindagem eléctrica em ambientes difíceis motivaram uma gradual substituição destes sensores em detrimento de muitos sistemas eléctricos convencionais. Em particular os recentes desenvolvimentos nas aplicações em deteção acústica vieram ajudar a suprimir uma necessidade no estabelecimento de um método estável e fidedigno para monitorizar estruturas em larga escala e efectuar medições em meios rigorosos.

Dada a profunda necessidade de uma afirmação das fibras óticas como elementos de alta fiabilidade com um desempenho superior aos tradicionais equipamentos eléctricos, esta dissertação proporciona um estudo sobre duas das mais importantes configurações em fibra ótica. Interferómetros Fabry-Pérot e redes de Bragg em fibra ótica foram desenvolvidos para deteção de ondas acústicas e os seus desempenhos comparados. Vários sensores foram desenvolvidos e caracterizados com o auxílio de um piezoelétrico como fonte acústica. Os resultados reforçam as boas perspectivas da utilização dos interferómetros Fabry-Pérot em micro-aplicações e realçam as qualidades das redes de Bragg como elementos muito sensíveis, flexíveis e possibilitadores de multiplexagem. A capacidade de detectar emissões acústicas típicas de processos de envelhecimento de várias estruturas tornam estes sensores adequados para monitorização não invasiva de estruturas de larga escala.

Palavra-chave: Sensores em fibra ótica; emissão acústica; Fabry-Pérot; Redes de Bragg em fibra ótica.

Table of contents

List of figures

List of abbreviations

EDFA – Erbium-doped fibre amplifier

EFPI – Extrinsic Fabry-Pérot interferometer

ESA – Electronic spectrum analyser

FBG – Fibre Bragg grating

FFT – Fast Fourier transform

FPI – Fabry-Pérot interferometer

FSR – Free spectral range

FWHM – Full width at half maximum

IFPI – Intrinsic Fabry-Pérot interferometer

LPG – Long-period grating

MI – Michelson interferometer

MZI – Mach-Zehnder interferometer

OFS – Optical fibre sensor

OSA – Optical spectrum analyser

PD – Partial discharge

PZT – Piezoelectric

SHM – Structural health monitoring

SI – Sagnac interferometer

SMF – Single mode fibre

SNR – Signal to noise ratio

SR – Sample rate

VI – Virtual instrument

WDM – Wavelength-division multiplexer

1 Introduction

In an era where rigorous safety requirements push forward the demand for resilient and reliable monitoring equipment, optical fibre sensors (OFS) have assumed a preponderant role as auspicious alternatives to the more conventional electrical devices. Its ease of integration and light weight combined with high sensitivity, robustness and noise immunity claimed much attention in the last decades and led OFSs to the vanguard of scientific research. This resulted in the appearance of a large array of solutions to sense varied physical quantities such as length, temperature, pressure or strain [1]. In particular, the field of acoustic sensing using optical fibres has seen investigation so as to develop precise instrumentation for monitoring of aging and degradation processes in large-scale structures including buildings, bridges and airplanes [2]. Following this trend, this study focuses on OFSs eligible to detect acoustic and vibrational signals with direct applications in diverse areas such as structural health monitoring, bioimaging, navigation and aerospace. Several sensors were developed with different sensing techniques in order for them to be compared and allow the understanding of their most suitable applications.

1.1 Motivation

Under the scope of diverse research motivations ranging from environmental concerns to new aerospace cutting edge components, the search for devices that allow accurate real-time monitoring in a wide variety of conditions is intense. In the context of acoustic sensing, piezoelectrics have long been preferred given their low cost and good sensitivity, leading to a successful appliance over the years. Despite these advantages, their difficulties in withstanding severe chemical environments together with low electromagnetic noise immunity and a frequently unavoidable set of electric cable apparatus present challenges in their integration in more demanding modern applications. Additionally, piezoelectrics present constraints under high temperatures since their crystalline nature dictates a well-determined Curie temperature as a limit, and prove to be inadequate when measuring static quantities due to charge leakage. All these limitations make piezoelectric sensors unsatisfactory solutions when reliability, hardiness and ease of incorporation are a requirement – situations like sensor embedding in aerospace wing components or in large induction motors and power lines. As a response to this need, OFSs were developed and applied

successfully in the last couple of decades since they address many of these concerns. Their high sensitivity, electromagnetic noise immunity, flexibility, ease of integration and multiplexing capabilities make them serious candidates for a gradual replacement of piezoelectric devices at the industrial and research level. Being chemically inert, OFSs can be safely exposed to otherwise potentially hazardous media such as fuel tanks or acidic environments, while being electrically passive means they can be integrated inside high-voltage structures for degradation monitoring. Still, and although OFSs outperform the traditional piezoelectrics, some problems remain to be solved if they are to reach a status that permits worldwide usage. Currently, understanding the mechanisms that occur in the interface area between the sensor and the measurand is one of the main challenges. Also, lowering the cost of the overall optical setup is of high importance if the use in non-high-tech applications is intended. Moreover, there is currently a lack of standardized descriptions of the sensor systems that allow non-familiarized industrial personnel to work with OFSs, although international guidelines and standardization activities have been under constant development.

It is under this prospect of further enabling OFSs to rise to the status of accurate, reliable and versatile sensing equipment by offering new tools for technological development that this dissertation has been done. By studying and characterizing OFSs as acoustic and vibration sensors one hopes to have contributed to this goal.

1.2 Dissertation objectives

This dissertation has the following aims:

- To develop and study interferometric setups designed for acoustic sensing. Special emphasis is given to Fabry-Pérot interferometers.
- To integrate fibre Bragg gratings (FBG) as sensing heads for acoustic sensing, together with an interrogation system.
- To apply FBGs in 3D woven composites for strain measurements.

1.3 Dissertation structure

This dissertation was structured so as to cover the three main steps that were taken during work: background, research and experiment, and applications. Two optical configurations were considered and in each one a standard approach of preliminary research, followed by experiment and subsequent analysis of results was taken. This enabled focusing on each subject and allowed a more accurate comparison

between the different techniques. Whenever possible, a chronological order was maintained so that one can have a clearer view on the course of actions.

In this first chapter an introduction to the subject of optical fibre sensors is given. The main reasons behind their choice as upcoming leading sensors for acoustic detection are stressed, as well as a brief description of this dissertation's outline.

Following this introduction, chapter two contains an overview relative to the state of the art of optical sensors applied to acoustic detection. Emergent devices are presented in the context of interferometric sensing, where a discretization of some of the more widely utilized configurations was done, along with their benefits and limitations. In all of them a short historical overview and a small summary of the solutions that are currently in the forefronts of technology are given, if applicable. Fabry-Pérot cavities and FBGs are also considered following the same outline since they are highly relevant as optical sensing solutions.

Chapter three concentrates solely on the study and development of Fabry-Pérot cavities. A theoretical introduction containing a brief mathematical description of this technique is given in the first place, setting a valuable background for the experimental investigation. Next follows a description of the experimental method for both the design and fabrication of the cavities as well as the experimental apparatus. Results and subsequent discussion are presented after, where some conclusions are drawn relative to the device's performance.

FBGs are considered in chapter four with a similar structure as has been taken in chapter three. After initially presenting the equations that conduct the behaviour of these sensors, the utilized setup for data acquisition is explained. The sensor's ability to detect acoustic waves is demonstrated subsequently, along with discussion and results regarding its functioning. Also shown are some preliminary results of an application of embedded FBGs in 3D woven composites for strain measurements. This subchapter contains a brief introduction to 3D composites as well as a description of the lay-up process. An analysis of reflected Bragg wavelengths during the infusion process is presented and a physical interpretation of the process is done as well.

The final chapter presents the conclusions that were drawn upon the obtained results. It assesses the feasibility of our sensors within the context of acoustic detection and sets a comparison between their performance and suitability. Expectations regarding future work on this field are presented in the end.

2 State of the art

As far as optical fibre sensors (OFS) are concerned, steady progress has been seen recently in the search for new sensing solutions; however, over the years different techniques experienced various degrees of attention by researchers, according mainly to their suitability for applications and their expected room for improvement at that time. Presented in the next section is a general overview of the major techniques to this date and their most recent developments. Some of these configurations may not be currently under the focus of vast research but were introduced here for their historical significance nonetheless.

2.1 Interferometric fibre optic sensors

The development of acoustic sensors resorting to interferometric processes has long been motivated by the technique's high sensitivity. Fibre optic interferometers operate by measuring the phase difference between two light beams that propagate along two different optical paths. This phase delay comes usually from fluctuations of the fibre's index of refraction that occur when the fibre is exposed to an external perturbation. In acoustic sensing, it is the acoustic wave that provides that effect when interacting with the fibre. Apart from phase detection, interferometers can also sense changes in intensity, frequency and bandwidth. This high sensitivity though can cause cross talk with temperature sensing, making thermal isolation related problems a common issue with interferometers. Strong temperature dependency usually means finding different schemes that can surpass this difficulty, adding unwanted complexity to the system.

OFSs for acoustic sensing were first conceived using interferometers some decades ago and ever since other optical solutions have been proposed. Yet, interferometric configurations are still used nowadays in a large array of applications. Lately optical interferometry has seen focused efforts to achieve miniaturization of optical components for micro-applications. In particular, in-line fibre applications are the new trend in this field as they provide integrability at a small scale.

2.1.1 Mach-Zehnder interferometer

Mach-Zehnder interferometry has been extensively used in temperature and pressure sensing benefitting from its good sensitivity and ease of integration [3,4]. Its mechanism utilizes a coherent source to generate an initial laser beam. The beam is then split by a coupler in two arms: the sensing arm and the reference arm. Both arms are then recoupled together creating an interference pattern that is received by a photodetector (Figure 2.1).

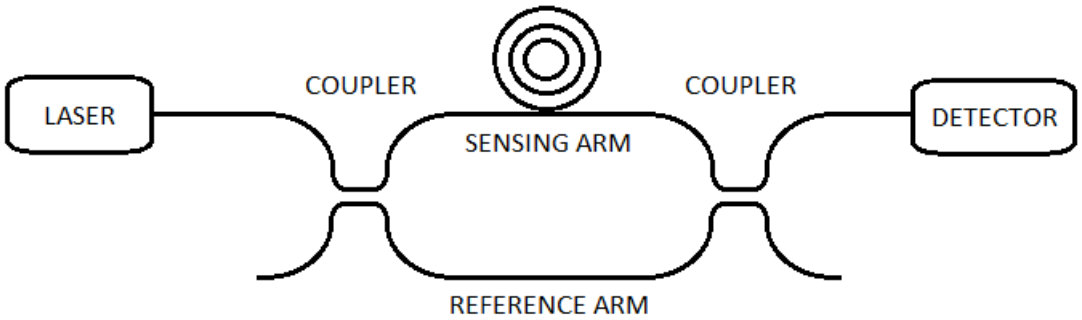

Figure 2.1 – Schematic configuration of a Mach-Zehnder interferometer. Light undergoes phase-shifts whilst travelling in the sensing arm, which will then form a fringe pattern when recoupling with the signal from the reference arm.

In their pioneering work in 1977, Bucaro et al utilized a Mach-Zehnder interferometer (MZI) as an acoustic sensor [5]. They showed that by exposing the sensing arm to an acoustic signal one could induce a change in the optical path, thereby assuring a phase shift when recoupling. This change would manifest itself as a resulting fringe pattern in the detected signal. From there they were able to infer the properties of the acoustic wave in the range of 40 Hz - 40 kHz with no significant fluctuations of sensitivity. Briefly after this discovery the same team presented an application of these acoustic sensors in optical fibre hydrophones. First they placed fibre optic coils in the sensing arm to act as a transducer, for they maximized the exposed length of optical fibre. After being immersed in a tank, these coils would then couple an acoustic signal that was propagating through the liquid medium.

This work opened doorways for the employment of acoustic sensing with optical fibres in marine engineering and navigation systems. The following decades saw a large account of studies being undertaken to further understand and apply Mach-Zehnder setups for interferometry-based hydrophones [6,7]. Presently, the call for smaller and more flexible sensing heads led research towards in-line configurations of the MZI. In an in-line core-cladding-mode interferometer the guided mode is split into two and propagates along both the core and the cladding (Figure 2.2). The cladding

mode gets exposed to external perturbations and acts as the sensing arm. Both modes are afterwards coupled back, forming a MZI in one single optical fibre. The splitting and coupling can be done through several procedures, the most common being the usage of tapered optical fibres (fibres in which specific zones of the fibre have their diameter reduced via heating and subsequent stretch), small segments of fibres with different diameters, or using long period gratings (LPGs). Chen et al applied an in-line MZI with 5.5 mm to capture acoustic waves generated from pulsed blood pressures to monitor heart-beat [8]. The device also worked as a low frequency vibration sensor, ranging up to 150 Hz.

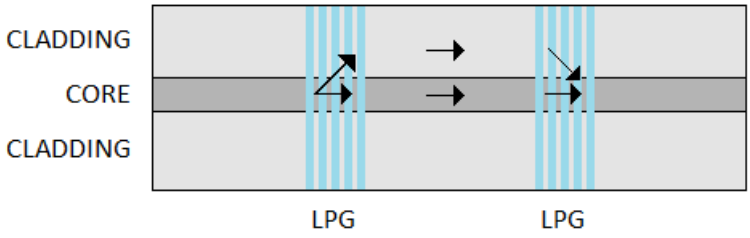

Figure 2.2 – Schematic configuration of an in-line Mach-Zehnder interferometer. Modes are propagated both along the core and the cladding of the optical fibre; splitting is done with the aid of a LPG.

Versatility is yet another advantage of the MZI setup. In 1988 Lagakos et al showed interferometers with increased flexibility using coatings made of composite structures [9]. More recently, Hernández-Serrano developed a more robust and flexible vibration sensor employing an in-line tapered MZI, managing to detect acoustic signals in the range up to 3 kHz [10]. Ease of fabrication and a simple interrogation system make this setup a practical choice for searching the characteristic frequencies of mechanical structures. The sensor was employed to detect the resonation modes of a cantilever.

Other domains, like acoustic imaging have also seen MZI being applied successfully. Paultauf et al. showed an application in tomography in which a 3D imaging method integrates a traditional MZI to detect acoustic waves produced by an object irradiated with a pulsed laser [11]. Final spatial resolutions between 100 and 300 µm have been reported, with the MZI presenting a sensitivity of 0.134 $rad \cdot bar^{-1} \cdot mm^{-1}$.

2.1.2 Michelson interferometer

Of all the interferometric sensing techniques, the Michelson interferometer (MI) is the less used for acoustic sensing. Ever since Imai et al. proposed the first setups in the 80's that very few developments have occurred to this date [12]. The interferometer is usually regarded as half of a Mach-Zehnder that includes two mirrors (Figure 2.3).

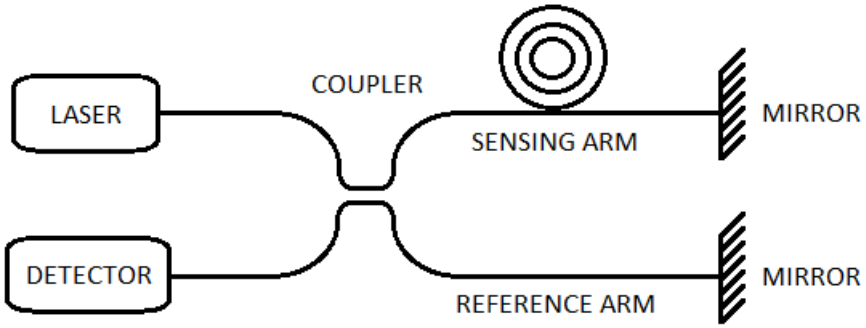

Figure 2.3 – Schematic configuration of a Michelson interferometer. The splitting and coupling of the beams occur in the same coupler after reflection in both mirrors.

The fringe pattern is acquired after an interference phenomenon between both rays coming from the sensing and the reference arm. Generally speaking the MI possesses more sensitivity than the MZI since the propagating beam in the sensing arm passes twice through the sensing head.

From an integration capability point of view, this sensing method has advantages over the MZI setup. In contrast to the latter, it allows the optical apparatus to be set in just one cluster, bundling together both the signal generation and signal detection equipment.

Regarding distributed sensing using optical fibres, Hong et al. proposed a system in which two Michelson interferometers were used as phase detectors [13]. An outside vibration would cause a phase shift in the sensing arm, and from there a real-time application could be developed for a movement detector to be installed in a security system. Nonetheless, improvements must be made before a real application can be made since a modest spatial resolution of just ±51m in a 4012m fibre was achieved.

Biomedical imaging technology engaging fibre optic sensors has been an active topic of research in the past few years. In this context, Michelson interferometers have been recently applied in photoacoustic tomography as pressure sensors for quadrature phase detection. This procedure eliminates the frequent need of tuning the laser wavelength for sensitive regions of the fringe pattern, an obstacle commonly found in Fabry-Pérot interferometers [14]. Although not directly an acoustic sensor, the MI in this setup allows for overall ultrasound detection with fast surface scanning properties that are vital for clinical applications. The device's sensitivity has been estimated to be $0.43/v$ Hz·Pa^{-1}, where v is the frequency of the photoacoustic wave, an achievement which is 5 to 10 times greater than other previously results reported elsewhere in literature.

2.1.3 Sagnac interferometer

Since its first developments in 1983 [15], Sagnac interferometry applied to acoustic sensing has been employed regularly in various applications given their ease of fabrication, simplicity of structure and sturdy response to demanding environmental conditions. They surpass the misalignment challenge encountered in conventional MIs and MZIs, leading to a more straightforward implementation and better noise shielding.

Although the classic configuration contained several plain mirrors, the modern Sagnac interferometer (SI) consists of a fibre optic ring configuration where two beams propagate in opposite directions with different polarization states (Figure 2.4).

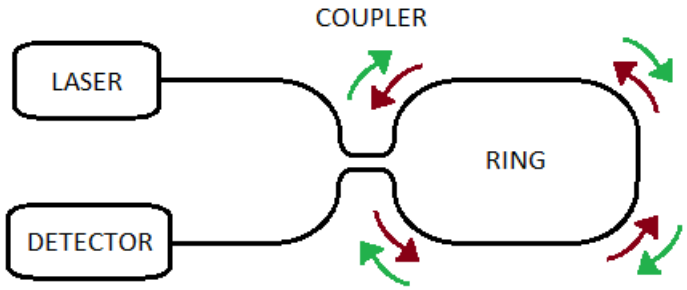

Figure 2.4 – Schematic configuration of a Sagnac interferometer. After counterpropagating within the ring the two beams interfere when reaching the coupler. The result is a fringe pattern obtained by the detector.

When continuously rotating the device in a specific direction, the optical path of one of the beams will become larger and the other one shorter, causing them to produce a fringe pattern when recoupled. Likewise other interferometric devices seen so far, coupling between the incident acoustic wave and the light beam will be responsible for changes in the refractive index of the fibre's core, introducing another phase-shift. By analysing the induced variations in the fringe pattern one can then obtain information about the acoustic wave.

After being initially applied in the context of rotational sensors, SIs were soon spotted for their advantages as acoustic sensors. Although the first applications were directed to improved hydrophones over the already existent MZI setups, it was in structural health monitoring (SHM) that SIs managed to found their biggest breakthrough. Several studies have reported SI-based sensors for microcracks and structural defects in large-scale concrete structures [16-18]. One particular recent paper reported the development of a leak detection system for long distance natural gas pipelines [19]. Improvements in pipeline monitoring are always highly praised since cracks and subsequent leaks are synonymous of high losses and environmental safety hazard.

The most recent trends seem to explore SIs as sensing agents for partial discharges (PD) [20,21]. These electrical discharges occur in high-voltage environments such as high-power transformers and can turn an insulation material into a conductive one. This phenomenon can damage the structure significantly and therefore there is much interest in designing sensing elements that could predict eventual failures and prevent the collapse of the whole structure. High voltage environments present challenges that limit the use of conventional acoustic detectors and hence attentions have been focused in OFSs, given their chemical inertness and electromagnetic shielding coming from their dielectric nature. SIs can be very useful for PD detection since they offer superior stability in face of thermal influences and can sense ultrasonic bursts in a high frequency range. Wang et al managed to design a PD sensor incorporating a SI with a high-frequency response of up to 300 kHz and capable of detection both partial discharges and weak corona discharges [20].

2.1.4 Fabry-Pérot interferometer

Fabry-Pérot interferometry has played an important role over the years in acoustic detection, given its high potential for micro-applications and miniaturization. A Fabry-Pérot interferometer (FPI) is essentially composed of two parallel highly reflecting surfaces and the interference pattern is obtained from the multiple superpositions of the transmitted and reflected beams on both surfaces (Figure 2.5).

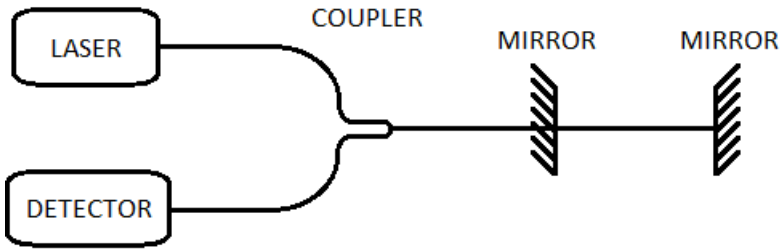

Figure 2.5 – Illustration of a Fabry-Pérot interferometer. Splices or in-built mirrors can act as mirrors, creating the cavity.

The spacing between the mirrors is called a Fabry-Pérot cavity, but in-line configurations can be achieved using splice regions as equivalent mirror surfaces. Whether or not the cavity is internal or external relatively to the optical fibre turns the FPI into an intrinsic or extrinsic interferometer (IFPI or EFPI, respectively). EFPIs are particularly relevant for acoustic sensing since they easily work as sensing heads [22,23].

Like the other interferometric setups, this technique was first applied to the development of optical hydrophones and marine applications, and this trend has been maintained until recently [24,25]. The latest devices are already resistant enough to withstand intense acoustic waves, an obstacle commonly found when working with more fragile piezoelectrics (PZTs). Kim et al have recently proposed a refractive index sensor based on a band-pass filter deposited on the tip of the fibre [25]. The resulting system presented itself as robust and capable to detect frequencies up to 1.56MHz, with a relatively low cost associated. Detection in the megahertz order of magnitude in liquids is of high-importance for industrial applications and medical imaging.

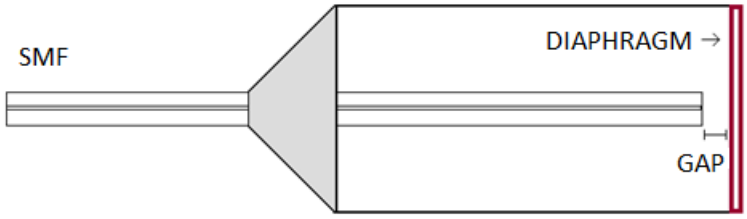

Figure 2.6 – Representation of an extrinsic Fabry-Pérot interferometer with a diaphragm as a reflective element. By encapsulating a single mode fibre (SMF) in this way, a Fabry-Pérot cavity is created in the gap between the tip of the fibre and the internal surface.

Plenty of studies have been made where diaphragms of different materials were incorporated as reflective elements (Figure 2.6). This configuration allows for significant improvements in the resulting sensitivity of pressure and ultrasound sensors. Graphene is one of the most studied materials for this application, with its high Young modulus and flexibility being the reason behind its choice [26]. Yet, the best results have been found with thin diaphragms of silver with 125 µm of diameter and 300 mm of thickness, with a sensitivity of 70.5 $nm \cdot kPa^{-1}$. Better results are hoped to be achieved if one manages to reduce the diaphragms thickness without affecting the range of detection. Another major breakthrough was done by Chen et al with the design of a FPI with just 1.5 µm thick chitosan diaphragm, exhibiting excellent physicochemical properties [27]. A response range between 20 Hz and 20 kHz with an impressive sensitivity of 0.002 $V \cdot mPa^{-1}$ was achieved.

In the field of acoustic detection for SHM, Fabry-Pérot interferometry has seen some important applications, especially in the detection of PDs. FPIs present themselves as excellent solutions to detect and locate precisely these discharges. Given the fact that they can resist these harsh environments, contrary to the ordinary PZTs, they can be integrated internally, largely reducing the signal noise and improving the device's sensitivity. Dong et al fabricated an advantageous multiple-point sensing system for weak PDs detection in power transformers from a diaphragm-based Fabry-

Pérot sensor, capable of a high-frequency response up to 200 kHz [28]. A more recent work demonstrated an EFPI with a quartz diaphragm and a short cavity length of 50 µm with the ability to sense signals in a frequency range up to a 2MHz, although it was applied to detect PDs at about 350 kHz [29].

2.2 Fibre Bragg gratings

Demonstrated for the first time in 1978 by Hill et al [30], fibre Bragg gratings (FBG) are microstructures printed directly in the core of the optical fibre. These microstructures are periodic modulations of the core's refractive index, making them act as reflective elements in a very specific and well-defined wavelength determined by the grating spacing. By analysis of the reflected signal one obtains information regarding the grating's period and the changes it has undergone. Since outside perturbations such as temperature variations, externally applied pressures or strains can significantly change the sensed core's refractive index, one can successfully design sensors for these parameters.

As one of the most promising developments in fibre optic sensing, FBGs have spurred much research during the past decades [31-33]. They have been applied with great success in ultrasonic detection ever since the first preliminary experiments in 1996/7 by Webb et al [32] and Fisher et al [33] for medical applications. Motivation for these developments has been centred on their notable properties and special suitability for less invasive medical procedures, given their compact structure, small diameter and chemical inertness inherent to optical fibres. Applications in biomechanics [34] and ultrasonic biopsies [35] have been reported, but perhaps the field in which FBG has had greater impact is in SHM, where many studies and applications have been undertaken in fields such as civil engineering, aeronautics, aviation and other engineering branches [36-38]. Chan et al showed the appliance of FBGs for SHM of Tsing Ma bridge, the world’s longest suspension bridge, employing a set of 21 FBGs multiplexed in three strands of fibres [36]. With an adjustable scanning rate of up to 20 kHz, a resolution of 1 pm and an accuracy of 10 pm, this remarkable system monitored strain in different parts of the bridge, revealing the dynamic response of the structure during train passages.

Acoustic emissions from structural damage are typically within the range between 1 kHz and 1 MHz and strains are on the micrometric order [39]. Detectors must then be able to respond in high-rate frequencies and possess great sensitivity,

properties in which FBGs overperform PZTs largely. In order to sense ultrasounds with FBGs it is necessary to employ signal demodulation and for this there are typically two available methods [40]. In the first one, a tuneable laser is set to emit in a steep region of the spectrum, where one can assume a linear regime (near the points that define the full width at half maximum (FWHM) for example). The detected intensity change will then relate to the ultrasound amplitude that is being exerted on the FBG. It has been demonstrated that the length of the FBG determines the maximum frequency of the detected ultrasound [2], with shorter fibres leading to a higher range of detection. On the other hand, shorter fibres also imply a less steep spectral gradient, which diminishes the sensitivity. To solve this compromise between sensitivity and range of detection, Rosenthal et al used phase-shifted FBGs (PS-FBG), decreasing the effective length of the grating and improving sensitivity [41]. Though highly sensitive this technique requires a tuneable laser, an expensive instrument not always available. The second solution uses a broad-spectrum light source instead of a laser. This allows for a cost reduction while making multiplexing an option. Adding a second filter is needed to demodulate the Bragg wavelength shift into optical intensity.

The conventional method for ultrasound sensing requires fixing the fibre along the structure that one wants to investigate. Although good sensitivity is achieved, this method has the inconvenient that the reflection peaks suffers fluctuations according to different deformations applied to the structure. Tsuda et al placed a FBG in a small moving platform set by the structure, creating an ultrasound sensor immune to deformation [42]. The study demonstrate that the reduction in signal to noise ratio (SNR) for the non-fixed sensors relative to the fixed ones was just 6 dB and that the ultrasound-induced strain detection was within the typical range of sub-micron strains.

The necessity to optimize sensors for reliable and precise monitoring of large scale structures has fuelled research with FBGs as sensing heads. Further developments are to be expected since these sensors have proved to be one of the best solutions available nowadays.

2.3 Final considerations

Optical fibre sensors can be moulded into many shapes and designs for different applications, but their transversal qualities as reliable, flexible and sensible devices remain a powerful trademark. Over the years they have been steadily pointed out as futurist sensors, but as the price of optical components decreases and more and more

applications are reported, general implementation of OFSs in our daily lives seems more likely.

Some interferometric configurations like the MI or the SI are progressively being left behind and only finding usage in niche applications, but MZI configurations still seem to be applied regularly in different fields.

On the other hand Fabry-Pérot interferometry seems to have the focus of its development in EFPIs, towards miniaturization of devices and microapplications. Their ability to be easily immersed in demanding environments should promise more future applications.

Increasing commercialization of FBG systems along with standardization of sensor characteristics make these devices the main propellers of OFSs study and research. Further applications of FBGs, especially in SHM, are to be expected.

3 The Fabry-Pérot interferometer

In the domain of interferometry applied to acoustic detection, Fabry-Pérot interferometers (FPIs) stand out as a preeminent solution. Thanks to high integrability, FPIs are feasible for withstanding continuous progress towards miniaturization, a current trend transversal to many technological fields. Acknowledging their relevance, an understanding of the physical principles behind FPIs together with an experimental approach involving acoustic characterization has been done. With this effort one aimed to get a clearer view of the importance and room for improvement of this interferometric device.

3.1 Fabry-Pérot cavities

The following section provides a theoretical treatment pertaining Fabry-Pérot interferometry. The main mathematical relationships that describe the behaviour and operation of these sensors are covered, as well as a fitting topic on acousto-optic coupling.

3.1.1 Principles and setup

The standard plane parallel Fabry-Pérot interferometer is an optical device constituted by two highly reflective planar mirrors. They stand perpendicular to the optical axis, with their reflective surfaces facing each other, distanced by some specific length – the Fabry-Pérot cavity.

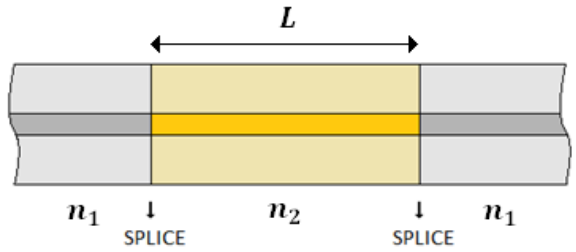

Figure 3.1 – Representation of a longitudinal section of a Fabry-Pérot cavity with in-line design, where two fibres with index n_1 and n_2 are spliced together. The splice regions guarantee some reflectivity in order to create the cavity with length L.

This design allows the setup to act as an optical resonator where multi-wave interference occurs. Using a coherent laser source, light is launched along the optical axis to the inside of the cavity through the first mirror. The beams are then repeatedly reflected within the cavity in a process resembling a feedback system. The waves eventually interfere at the end of the cavity forming a well determined fringe pattern.

Apart from this conventional configuration, FPIs cavities can also be designed by splicing the ends of two segments of optical fibre with index n_1 to a fibre with index n_2 (Figure 3.1). This assures some reflectivity R in the splice region which leads to multiple reflections in the cavity (i.e. the fibre with refractive index n_2). Hence, the theoretical treatment for the standard mirror setup can also be applied to the in-line design. This configuration is nowadays particularly important and will be treated with more detail further. As already seen, other Fabry-Pérot configurations can be achieved, for instance using external diaphragms where the cavity is made of a small air gap between the tip of the fibre and the diaphragm itself.

3.1.2 Multi-wave interference phenomena

Let us assume a light beam travelling parallel to the optical axis along a segment of optical fibre pertaining to an in-line FPI, like the one depicted in Figure 3.1. For the sake of simplicity, the cavity is treated as being lossless. After entering the cavity through the first splice, a light beam propagates along its length L until it reaches the second splice, where it is partially reflected back. Then, as the reflected light beam travels backwards, it is reflected again in a similar fashion in the first splice, this time regaining its original direction of propagation. Thus an interference pattern is obtained after light transits through the second splice, as a result of the interference between the beams that passed through the splices without suffering reflection and the beams which suffered multiple reflections within the cavity. In the process of undergoing two reflections in one round trip inside the cavity, a light beam acquires a certain phase shift, determined by

$$\delta = 2kn_{eff}L \tag{3.1}$$

where n_{eff} is the effective refractive index of the fibre that constitutes the cavity, k is the wave vector defined as $k = \frac{2\pi}{\lambda}$ and λ is the wavelength of the laser. Neglecting any absorbance effect that takes place in the splice regions, the intensity distribution

obtained of the transmitted pattern after multiple interferences (also called transmittivity) assumes the shape of an Airy function:

$$T = \frac{I_t}{I_i} = \frac{1}{1 + Fsin^2\left(\frac{\delta}{2}\right)} \tag{3.2}$$

$$F = \frac{4R}{(1-R)^2} \tag{3.3}$$

where R is the reflectivity of the splice, I_t and I_i are the amplitudes of the transmitted and incident waves respectively, and F is an auxiliary function introduced for simplification, generally referred as the F parameter or as the coefficient of *finesse*.

Some special cases of the Airy function are of particular interest, namely when it presents a minimum or a maximum, corresponding to the event of destructive or constructive interference, respectively. In order to attain constructive interference the various reflected waves must be in phase upon reaching the end of the cavity. Formally speaking, the reflected waves have to fulfil the condition that the different phases acquired during multiple reflections must add to be a multiple of 2π:

$$\delta = 2\pi m \tag{3.4}$$

where m is an integer. Likewise, destructive interference is represented as valleys in the graphic and occurs when the phase difference of two incoming waves is a multiple of π:

$$\delta = \pi m \tag{3.5}$$

The transmittivity function contains two useful quantities that serve as quality factors for the FPI: the free spectral range (FSR) and the full width at half maximum (FWHM). The FSR is a measure of the sensitivity of the device and provides the range of frequencies or wavelengths that can be observed. It can be defined as the spacing in optical frequency or wavelength between consecutive peaks of interference:

$$\Delta\nu_{FSR} = \frac{c}{\Delta\lambda} = \frac{c}{2n_{eff}L} \tag{3.6}$$

$$\Delta\lambda_{FSR} = \frac{\lambda^2}{2n_{eff}L} \tag{3.7}$$

where c is the speed of light in vaccum. The FWHM is in its turn a key parameter to understand the spectral resolution and measure the sharpness of the fringes. The FWHM is also a measurement of the resolving power of the instrument, i.e. the capability of distinguishing two closely separated peaks.

Assuming high reflectivity in the splice regions and a null transmitted intensity between, it is reasonable to approximate $T = 0.5$ at the half maximum points. Thus, by introducing these simplifications the phase difference can be described in a simpler way by rewriting equation (3.2) in respect to δ:

$$\sin\left(\frac{\delta}{2}\right) = \frac{1}{\sqrt{F}} \tag{3.8}$$

For small values of δ (which is generally the case) it is safe to apply the small angle approximation $\sin\theta \approx \theta$ and obtain $\delta = \frac{2}{\sqrt{F}}$ for the phase change from the peak to the point of half maximum. The FWHM is hence twice that phase difference:

$$\delta_{FWHM} = \frac{4}{\sqrt{F}} \tag{3.9}$$

Although the FSR and the FWHM are good quality gauges for FPIs, another quantity has been defined as the main figure of merit: the *finesse.* It is the ratio of the separation between adjacent maxima over the FWHM:

$$\mathcal{F} = \frac{2\pi}{\delta_{FWHM}} = \frac{\pi\sqrt{F}}{2} \tag{3.10}$$

Substituting in equation (3.10) the expression for the coefficient of *finesse* one obtains an expression for the *finesse* as a function of the reflectivity of the splices only:

$$\mathcal{F} = \frac{\pi\sqrt{R}}{1-R} \tag{3.11}$$

In the optimum case of perfect splices with maximum reflectivity the *finesse* is expected to diverge to infinity. Real splices though are imperfect and always introduce losses which lead to broadening of the transmittivity function, resulting in a finite value for the *finesse* (Figure 3.2). Moreover, other problems like alignment difficulties that

shift the direction of the beam away from the optical axis, non-collimated beams or impurities can decrease the quality of the device and also induce broadening in the spectrum.

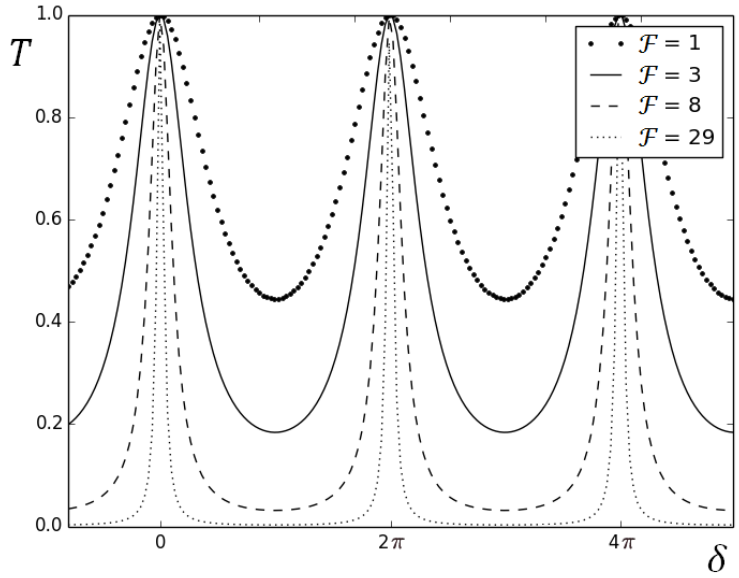

Figure 3.2 – Dependence of the transmittivity function on the phase difference for different values of the *finesse*. Peak values occur at 2π intervals. Peaks sharpen with the increase of reflectivity, i.e. with the increase of the *finesse*.

Table 1 – Summary of equations that describe the behaviour of a Fabry-Pérot interferometer. This set of quantities allows for a characterization of the device and gives a theoretical evaluation of its performance.

Transmittivity	$T = \frac{1}{1 + Fsin^2\left(\frac{\delta}{2}\right)}$
FSR	$\Delta\nu_{FSR} = \frac{c}{2n_{eff}L}$
FWHM	$\delta_{FWHM} = \frac{4}{\sqrt{F}}$
Finesse	$\mathcal{F} = \frac{\pi\sqrt{R}}{1-R}$

Armed with this theoretical description of the interferometer it is now possible to compare different FPIs according to various quantities and withdraw conclusions about their performance (Table 1). The derived equations are suitable for both the traditional etalon configurations with a transparent plate and the demonstrated in-line designs.

3.1.3 Acousto-optic effect

Acousto-optics is the field in physics that studies the interaction between phonons and photons. In order to understand the effect that an external perturbation such as a pressure wave may have on an optical sensing head, it is most convenient to have a solid understanding on this matter of how light and sound interact with each other.

When an acoustic wave propagates through an elastic medium it can be regarded as local pressure variations that spread through the material. Upon interacting with an optical sensing head the acoustic wave will cause changes in the optical path perceived by the light beam. For interferometric sensors, interest is focused in phase changes since this will enable the acquisition of interferometric patterns.

The phase of a light wave passing through a segment of optical fibre is:

$$\phi = \xi L = \frac{2\pi}{\lambda} n_{eff} L \tag{3.12}$$

where ξ is the propagation constant, λ is the wavelength, n_{eff} is the effective refractive index of the optical fibre's core and cladding, and L is the physical length of the fibre segment. The induced phase change can be mathematically expressed as:

$$\Delta\phi = \xi\Delta L + L\Delta\xi \tag{3.13}$$

$$\Delta\phi = \Delta\phi_1 + \Delta\phi_2 \tag{3.14}$$

where one designated $\Delta\phi_1 = \xi\Delta L$ and $\Delta\phi_2 = \Delta\xi L$. The first term relates to the physical elongation of the fibre due to the applied strain which is simply given by $\Delta L = \varepsilon L$, where ε is the strain. Therefore the first term takes the form of:

$$\Delta\phi_1 = \xi\varepsilon L \tag{3.15}$$

The second term refers to changes in the propagation constant which can come from two different sources: variation of the refractive index or a change in the fibre's diameter ΔD:

$$\Delta\xi = \frac{\partial\xi}{\partial n}\Delta n + \frac{\partial\xi}{\partial D}\Delta D \tag{3.16}$$

Theoretical description of the strain-optic effect yields a well-known expression for the change in the refractive index resulting from longitudinally applied strain [43].

$$\Delta n = -\frac{n^3 \varepsilon}{2}[(1-v)p_{12} - vp_{11}] \tag{3.17}$$

where v is the Poisson's ratio and p_{11} and p_{12} are elements from the strain-optic tensor p_{ij}. While the derivative of ξ with respect to n is calculated straightforwardly as $\frac{\partial \xi}{\partial n} = \frac{2\pi}{\lambda} = k = \frac{\xi}{n}$, the term $\frac{\partial \xi}{\partial D}$ is not so trivial. However, this term is very small compared to the former and can be neglected, as has been reported elsewhere in the literature [43]. Therefore the second term is presented as:

$$\Delta \phi_2 = -\frac{n^2 \varepsilon L \xi}{2}[(1-v)p_{12} - vp_{11}] \tag{3.18}$$

Hence, the final equation for the phase change is given by:

$$\Delta \phi = \varepsilon L \xi \left\{1 - \frac{n^2}{2}[(1-v)p_{12} - vp_{11}]\right\} \tag{3.19}$$

3.2 In-line Fabry-Pérot sensors

Fabry-Pérot interferometry sees applications in the branch of acoustic detection mainly because of its high sensitivity and small scale apparatus. In particular, in-line structures are interesting configurations whose development is underpinned by valuable benefits such as ease of alignment, good coupling efficiency and high stability. In this subchapter in-line Fabry-Pérot cavities are explored as acoustic sensors by producing and characterizing sensing heads with the aid of a piezoelectric.

3.2.1 Experimental setup

Several sensing heads were produced at the lab to serve as FP cavities. A glass fibre made of Suprasil F300 synthetic silica coated with UV-Acrylate PC370AP was chosen as the propagation medium of the cavity because of its high-quality and low-impurity grade attributes that grant the final fibre with low-loss properties.

The method of fabrication consisted in splicing both ends of a segment of Suprasil F300 fibre to a SMF optical fibre. Such procedure required a modern fusion splicer device allowing manual splicing between two fibres with approximate diameter. Two different fusion splicers were employed according to the specifications of the desired splices: a Sumitomo Electric Type – 71C Direct Core Monitoring Fusion Splicer for splices involving regular SMF optical fibres, and a Fujikura FSM – 60S Arc Fusion Splicer when splicing between two different fibres was needed, taking advantage of its more intuitive and easy-to-use manual splicing. The procedure required caution, as to prevent air bubbles from setting in and to guarantee a homogenous splice as much as possible. Since splices acted as the conventional mirrors for a Fabry-Pérot interferometer any major physical defects in this area would introduce high losses, which in turn would lead to a decrease of sensitivity of our sensors. The sensors were posteriorly attached to a steady cardboard and fixed with duct tape to the optical table whilst slightly tensioned.

The first steps aimed to verify the correct operation of our system. Confirming the existence of a fringe pattern as well as determining the quadrature point were fundamental aspects for the characterization of the sensors.

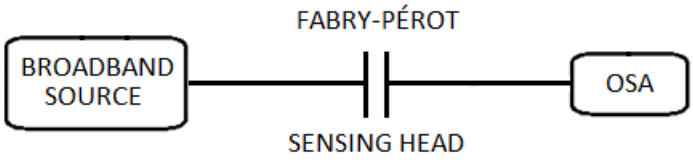

Figure 3.3 – Simple scheme for visualization of the fringe pattern of a Fabry-Pérot interferometer.

The FPs worked in transmission mode, a feature which made the utilized setup for acoustic characterization rather simple. Visualization of the interference fringes was attained by launching light into the fibre with a broadband light source through one end of the SMF fibre. After suffering multiple reflections within the cavity, the transmitted beam was received using an optical spectrum analyser (OSA) (Figure 3.3). Two different OSA devices were used throughout the development of this thesis with slightly different characteristics: an Advantest Q8384 Optical Spectrum Analyser with a maximum resolution of 0,01 nm and an Ando AQ-6315B, with a maximum resolution of 0,05 nm. Averaging processes were carried out (point by point or sweep averages) when necessary to soothe noise signals. Normalized signals in respect to the source were then obtained which allowed knowing the quadrature points with which the laser should be tuned to achieve maximum sensitivity.

The experimental setup for the acoustic characterization resembles the one used for visualization of the fringe pattern, but the source and data acquisition system were replaced by other more suitable equipment (Figure 3.4).

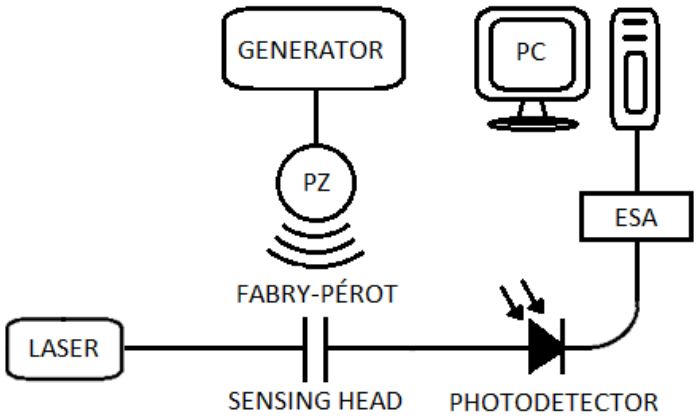

Figure 3.4 – Setup for acoustic characterization with Fabry-Pérot sensing heads. Laser emission was set to the quadrature point in order to guarantee maximum sensitivity.

The light source was a tuneable laser from Santec, class 3R, model TSL – 210V capable of delivering light in a very narrow bandwidth in the range 1500-1620 nm. After travelling through some length of regular Corning® SMF-28®, light was then set to undergo transmission through the splice region into the cavity. Here it was exposed to the exterior acoustic perturbation while propagating back and forth along the cavity.

The sensing heads were exposed to the PZT by applying the latter directly on top of them. Subsequently small weights were also added on top of the PZT to assure physical contact between the source and the sensor and in this way maximize the acousto-optic coupling. The PZT was connected to a Stanford DS345 30 MHz function generator, a stable instrument which allowed frequency sweeps in a large range.

The ensuing process would see the light beam leaving the cavity through the final splice and being collected by a photodetector. Analysis of the transmitted beam was now possible with an electronic spectrum analyser (ESA) and a homemade LabView virtual instrument for data acquisition.

The ESA board employed was a high resolution digitizer from National Instruments, model PCI-5122. It controlled a sample rate of 100 MS/s in real-time and a resolution of 14-Bit sampled simultaneously on two channels and operated in a bandwidth of 100 MHz with noise and antialiasing filters.

The LabView program performed a fast Fourier transform (FFT) over the real-time acquired signal according to different user inputs regarding sampling rate, resolution or averaging. The final output presented a spectrum in which one could

distinguish the outside perturbation as an independent phenomenon among the background noise.

The used VI (virtual instrument) lacked an automation routine that would connect the generator as a trigger element in the LabView program. This meant that the user had to manually sweep the frequencies one by one, making it a slow process. One single sweep could take typically somewhere between ten seconds to one minute or more, according to the desired specifications. Sweeps intended to cover large frequency ranges with short steps meant that sometimes one had to spend two to three hours characterizing a single sensor.

3.2.2 Results

A verification of the right state of operation of the laser was done in order to assure a correct characterization of our sensors and to confirm the feasibility of the upcoming results. To this end a PZT was set to a specific frequency and placed directly on top of the sensor head, using the experimental setup displayed on Figure 3.4. Sampling of the signal's amplitude relative to each specific frequency followed, while varying the laser output power (Figure 3.5).

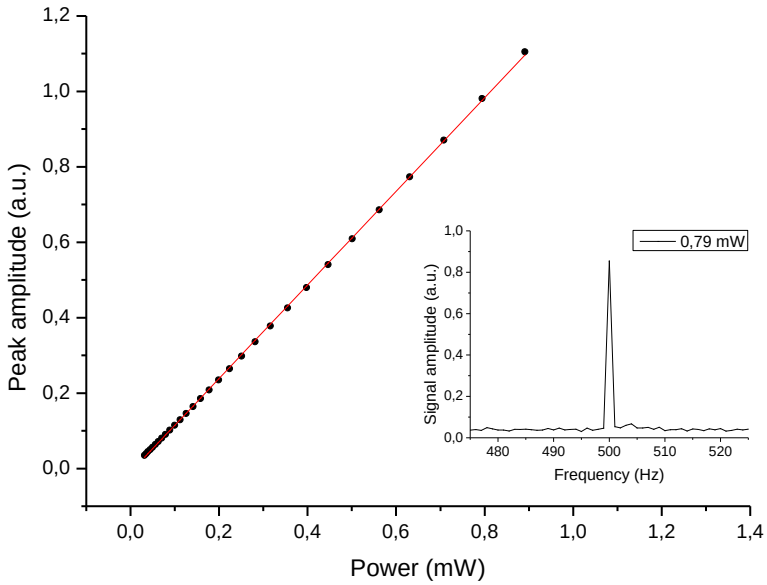

Figure 3.5 – Peak amplitude sensing as a function of the applied laser power for a constant PZT frequency of 500 Hz and $\lambda = 1560{,}000$ nm, using a 8,5 mm long Fabry-Pérot cavity. *Inset:* Peak height profile for 0,79 mW applied laser power.

Early experiments involved fabricating sensors 30 to 150 millimetres long. Though easy to produce and integrate due to good handling, these rather large sensors yielded unclear fringe patterns, not showing distinct fringes or periodic behaviour. As the relationship between sensor length and sensitivity started to be

understood, effort was placed in developing smaller sensors, with the smallest sensor fabricated having 0,5 mm of length. For sensors with less than 10 mm it became increasingly hard to fabricate ever smaller sensors as one tried to manoeuvre very tiny segments of fibre with mechanical cleavers and fragile splices.

The most interesting results came indeed from the smallest sensors, namely the ones with 0,5 mm, 1 mm and 3 mm of length, all of them showing well defined fringe patterns (Figure 3.6). Stability in the fringe amplitude can be compared, when it is easy to note that sensor length relates to this parameter. Thus the 5 mm sensor shows less signal amplitude oscillation while in the other end the 3 mm sensor presents a more erratic behaviour than the other two. Also, between these three it is possible to see that there is a tendency of having a smaller fringe period with increasing sensor length.

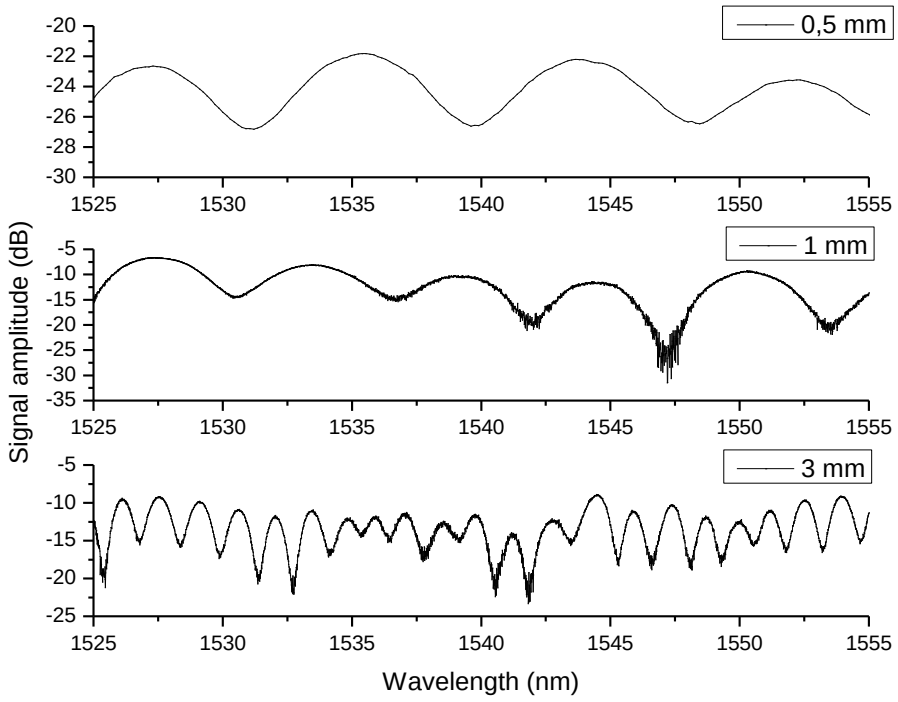

Figure 3.6 – Fringe patterns for Fabry-Pérot cavities with 0,5 mm, 1 mm and 3 mm. Different fringe periods and signal oscillations can be related to sensor length. Sampling OSA specifications: *0,5 mm* – resolution: 0,01 nm; point average: 8; sweep average: 16 | *1 mm* – resolution: 0,05 nm; point average: 1; sweep average: 8 | *3 mm* – resolution: 0,05 nm; point average: 1; sweep average: 8

The studied sensors with lengths between 75 mm and 210 mm showed a new spectrum when compared with the smaller cavities (Figure 3.7). Large main fringes appeared which were not dependent on cavity length. In this case the cavity comprises both the core and the cladding since lights travels in both mediums. These cavities present the same behaviour as sensors of the Figure 3.6.

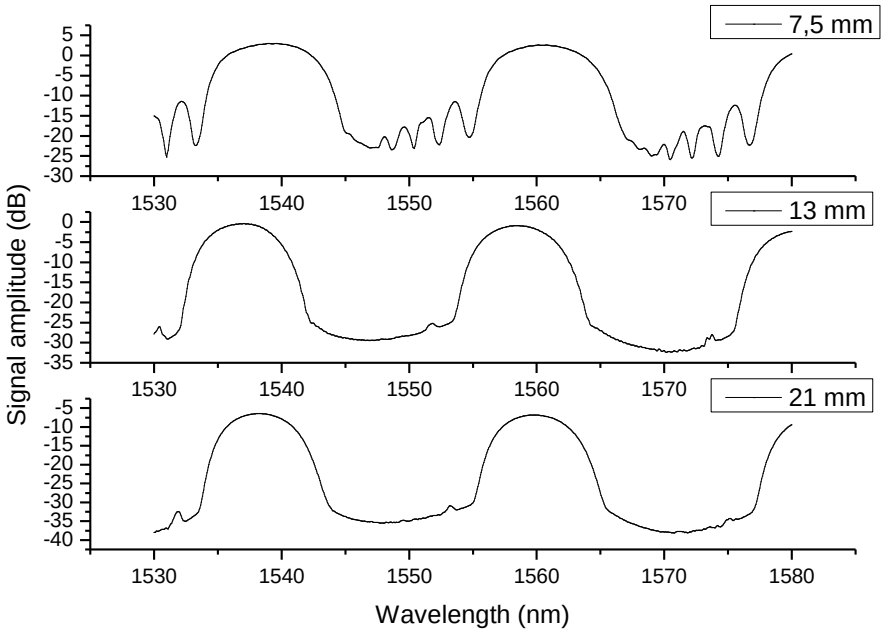

Figure 3.7 – Fringe patterns for Fabry-Pérot cavities with 7,5 mm, 13 mm and 21 mm. Fringe behaviour is non-sinusoidal, aperiodic and unstable. Sampling OSA specifications: *0,5 mm* – resolution: 0,01 nm; point average: 8; sweep average: 16 | *1 mm* – resolution: 0,05 nm; point average: 1; sweep average: 8 | *3 mm* – resolution: 0,05 nm; point average: 1; sweep average: 8

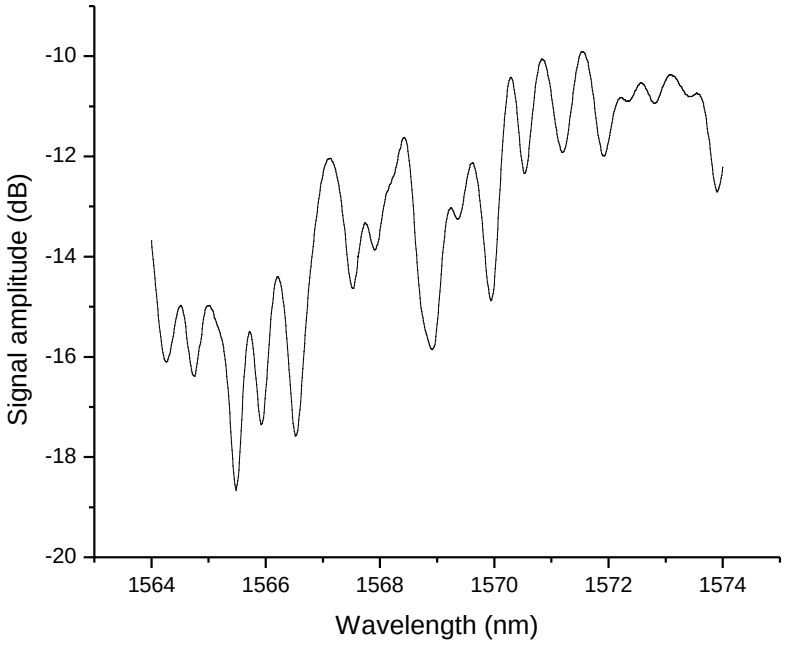

Figure 3.8 – Fringe pattern for a Fabry-Pérot cavity with 98 mm. Fringe amplitude oscillates heavily and it is difficult to establish a well-determined period for the pattern. Sampling OSA specifications: resolution: 0,2 nm; point average: 1; sweep average: 1

Sensors with even greater length presented aperiodic spectrums, resulting from multi-interference of light-waves on the fibre's cladding, forming a multimodal interferometer (Figure 3.8).

The relationship between the fringe period and sensor length was studied for all the developed sensors (Figure 3.9). Since it was impossible to determine fringe periods for the larger sensors produced, one could only plot $\Delta\lambda\ (L)$ for lengths up to 8 mm.

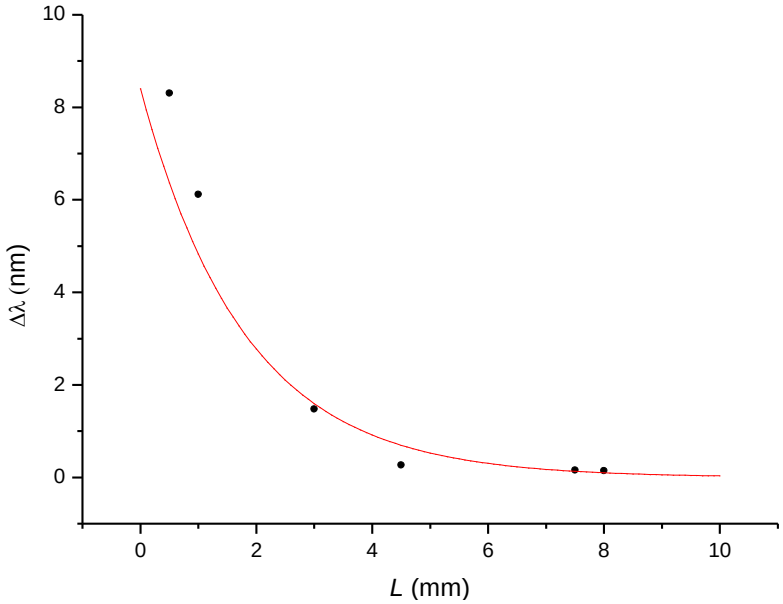

Figure 3.9 – Fringe period Δλ as a function of sensor length L for several Fabry-Pérot sensing heads.

It is possible to see an inverse relationship between sensor length and the fringe period when taking into account the sensors with 8 mm or less. For sensors larger than 8 mm this relationship is unclear, as is also unclear the fringe pattern itself.

The acoustic characterization of the sensing heads was achieved by exposing the sensor heads to a large range of varied and discrete frequencies. Limitations on the range of characterization were imposed mainly by the LabView VI, cutting of frequencies above 500 kHz due to the available computer RAM, and by the PZT, whose impedance response indicated several resonance frequencies starting from 60 kHz. The frequency step applied was typically of 2 Hz, a value chosen after noticing that meaningful frequency oscillations in the spectrum usually spanned a few hundred hertz and also because this setting allowed one to see amplitude decays around the peak frequency.

The gathered results prior to the implementation of a proper averaging method in the LabView VI led to only qualitative evaluations of the correct functioning of the tested sensors. After its implementation, efforts were centralised in the characterization of the smaller and more promising sensors, purposely neglecting the others. A quick visual comparison between results with and without averaging can confirm this point (Figure 3.10).

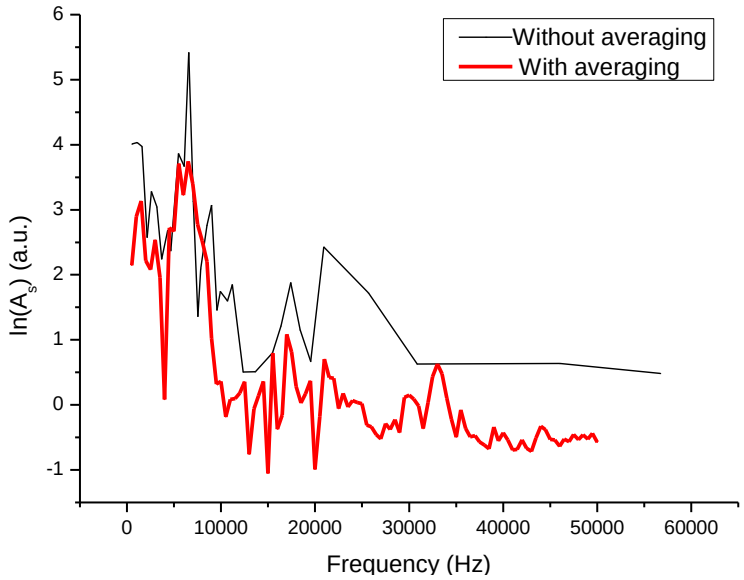

Figure 3.10 – Spectrum of the detected peak amplitudes for a 13 mm Fabry-Pérot sensor with and without the application of averaging methods.

The frequency response of the three most promising sensors showed some similarities between them (Figure 3.11). It is worth noting that at some particular frequency intervals (e. g. 15-18 kHz, 43-46 kHz, 51-53 kHz) all the sensors responded with greater signal amplitude.

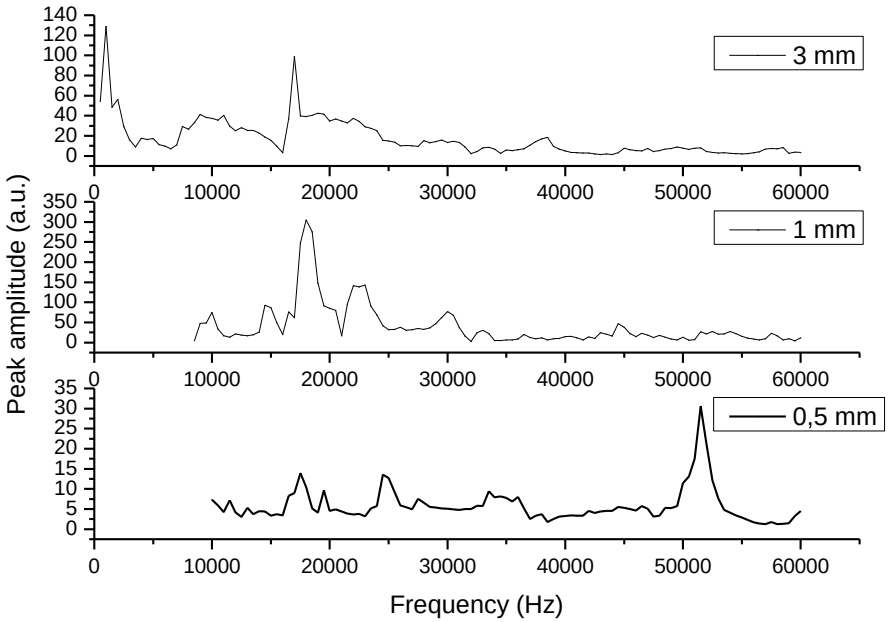

Figure 3.11 – Spectrum of the detected peak amplitudes for three different Fabry-Pérot sensing heads. S*ample rate*: 2M/s ; *iterations:* 100 ; *points per iteration:* 1M. Quadrature points: *0,5 mm*: $\lambda = 1562{,}620$ nm | *1 mm*: $\lambda = 1564{,}500$ nm | *3 mm:* $\lambda = 1560{,}300$ nm. Laser power: *0,5 mm*: -20,90dBm | *1 mm*: +1,45 dBm | *3 mm:* -8,00 dBm

Acoustic characterization of the smallest sensors revealed disparate values for the SNR (Table 2), with splice quality certainly having a decisive effect on them.

Nevertheless, all of them indicate clearance of signal relative to the present background noise.

Table 2 – Signal-to-noise ratios for sensors with 0,5 mm, 1 mm and 3 mm and respective applied laser power. The SNR was calculated as the squared ratio between the signal and noise root mean squared amplitudes.

Sensor (mm)	*SNR (dB)*	*Laser power (dBm)*
0,5	13	-20,90
1	33	+1,45
3	29	-8,00

Regarding the temporal response of the sensors, the collected data indicates a stable response in the range 110-130 mV. It is from this response that it is possible to perform a FFT and obtain the acoustic spectrum for each sensor.

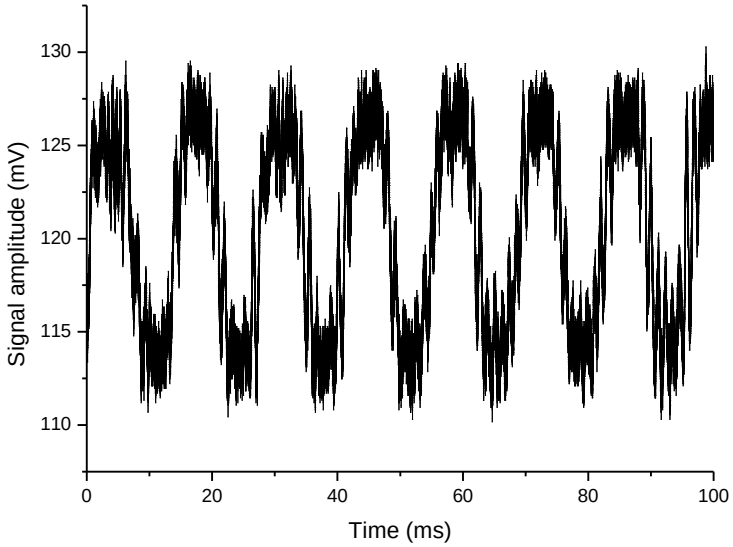

Figure 3.12 – Time response for a Fabry-Pérot cavity with 0,5 mm of length with an applied PZT frequency of 56 kHz

3.2.3 Discussion

All the experiments that were carried point to the fact that the smallest sensing heads display the best interference fringes. One likely cause for this effect is the fact that since the optical path sensed by the propagating light is shorter in smaller sensing heads, then also smaller is the portion of light that is dispersed and lost. This in turn translates into a higher fraction of light propagating back and forth along the cavity, thus magnifying the resonance effect inside the sensing head. Fringes from the 0,5 mm sensor oscillate less than their counterparts and fittingly the 1 mm sensor appears to

show more stability than the 3 mm sensor. Sensors with even greater length start to have an even more erratic behaviour.

Apart from stability, fringe periodicity relates also, and more importantly, to sensor length. The results in Figure 3.9 are in accordance with what would be expected: smaller sensors have higher periods. This is particularly true and easy to confirm with the smaller sensors since the bigger ones (larger than 8 mm) fail to provide clear fringe patterns in the first place.

Sensors with an intermediate size produced interesting but yet complex fringe patterns. Main patterns showing large fringes were composed by smaller oscillations, sometimes difficult to distinguish from noise oscillations. This behaviour is due to light travelling both in fibre's core as in the fibre's cladding, experiencing different indexes of refraction. It seems reasonable to assume the smaller oscillations as being the real fringe pattern since they follow the fitting line in the $\lambda(L)$ graph.

When studying the acoustic response the best results were obtained with the smallest sensors developed, creating a logical link between fringe pattern quality and acoustic sensing performance. The production and testing of these three sensors in similar conditions allowed concluding more distinctly about their performance. The ideal case had the sensors displaying a flat and predictable response to the whole array of scanned frequencies together with a high SNR, but the real case deviates largely from this desirable pattern. The sensors show a wiggling spectrum, with amplitudes varying significantly within short frequency intervals. For the purposes of sensing it is not critical that the sensors behave in this way, whereas the important feature is a high SNR in the desirable frequency range so that the signal can be unravelled from the background noise. A further calibration according to the normalized spectrum can enable the sensor to equally perceive signals with the same amplitude but different frequencies.

The fact that the wiggling of the spectrum is still due to too much instability not fully compensated by averaging can be in turn a big setback for real-purpose applications. Such an effect could compromise the speed and reaction time of a real system in which one may assemble the acoustic sensor, given that to sense more accurately the signal's amplitude the sensor needs more time of data acquisition. It can also affect the locating of acoustic bursts characteristic of structural cracks if these are too brief, though it does still allow for the detection of the acoustic emission itself.

The SNR exhibited by the smallest sensors is very reasonable, opening ways for their real application. Table 2 shows that the 1 mm sensor had a greater SNR than the 0,5 mm or the 3 mm sensor, but this was only due to the applied laser power being

very large compared to the other sensors. This was required because the 1 mm had high loss and so it was necessary to set the laser power to higher values so that the 100-120 mV signal could reach the photodetector. This in turn led to increasing power travelling inside the cavity and thus enhanced the sensed frequencies.

When comparing these three sensors it is apparent that in some peculiar frequency intervals all the sensors exhibit above-average amplitudes for the sensed signal, such as the 15-18 kHz interval. The fact that three sensors with different lengths reveal these resonance-type incidents seems to give a clue that the origin of the resonance comes from sources outside the cavity, though it is hard precise something beyond that. It can be anything nearby the setup that senses the PZT's frequency and reacts positively, feed backing the sensing head with the same frequency.

It is also worth noting that among the three sensors the 0,5 mm and 1 mm seem to have more similarities in their frequency response between them than with the 3 mm sensor, a behaviour most likely motivated by their shorter length difference. This might indicate that spectrum changes induced by splice losses and other sources of perturbations are not as dictating when it comes to the acoustic response as initially thought.

According to the temporal response displayed by all the sensors, the devices exhibit high stability. Real-time analysis of the temporal response allowed for the observation of instability caused by outside perturbations as these data would oscillate heavily. Steady temporal responses give more credibility to the FFTs that are obtained thereafter and hence are an important aspect when acoustically characterizing Fabry-Pérot sensors.

4 Fibre Bragg grating sensors

Widely regarded as the most promising branch of optical fibre sensors (OFS), fibre Bragg gratings (FBGs) have been employed with great success in recent applications spanning distinct technological demanding fields, from novel delicate medical procedures to structural health monitoring (SHM) in composites for aerospace parts. Such topicality has surged an interest to evaluate FBGs in the context of acoustic detection and to compare it to other sensing methods. Reported in this section is the characterization of a FBG laser sensor and its feasibility as acoustic sensors. Applications in structural health monitoring (SHM) are also discussed, including strain measurements with embedded FBGs in 3D woven fabrics.

4.1 Description of a FBG

By subjecting a section of the core of an optical fibre to an external periodic modulation one can locally modify its refractive index. These fluctuations in the core's refractive index can be achieved with a variety of laser-based techniques, usually involving interferometric methods or photomasking. Using an intense laser source in the UV region, a small segment of the fibre senses the beam intensity distribution and undergoes changes in its refractive index according to that same profile. The printed pattern usually takes the form of a quasi-sinusoidal modulation of the core's original refractive index n_c. A common refractive index profile is shown schematically in Figure 4.1, although as already seen here there are PS-FBG that have aperiodic gratings.

Bragg gratings behave as selective mirrors, reflecting highly in a well determined frequency band in the spectrum and transmitting all the remaining wavelengths. The spectral behaviour of a FBG and its principle of operation are schematically presented in Figure 4.2.

In its free state, each FBG has a very narrow reflection bandwidth around the peak which is directly dependent to the grating's spacing. This relationship is shown in Bragg's formula

$$\lambda_B = 2n_{eff}\Lambda, \tag{4.1}$$

where λ_B is the reflected Bragg wavelength, n_{eff} is the effective refractive index of the core after modulation and Λ is the grating's spacing. According to the last expression,

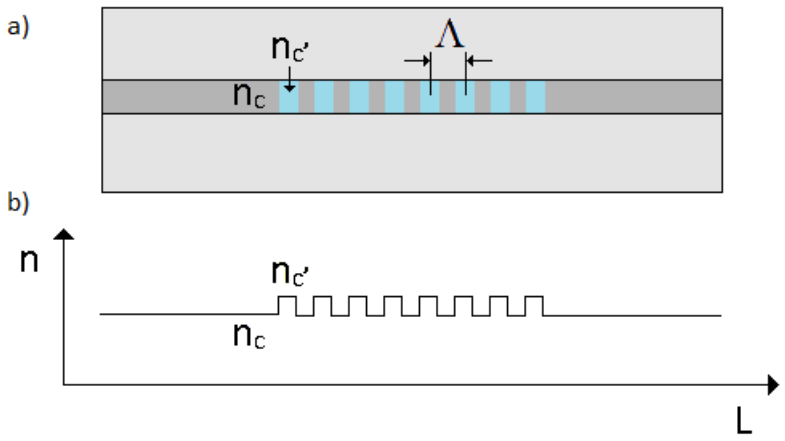

Figure 4.1 – General scheme of a FBG; a) 2D representation of a fibre optic segment containing a FBG; b) FBG refractive index profile n as a function of length L, where n_c denotes the pure refractive index of the fibre n_c' the modified refractive index and Λ as the grating's period.

one expects a spectral shift in the detected Bragg wavelength when tensional or compressive forces are applied longitudinally to the FBG, since they would cause a change in the grating's length. Indeed, by simply physically tapping gently a FBG during real time monitoring (i.e. inducing slight changes in the grating's length) one can shift the Bragg wavelength significantly up to a few nanometres.

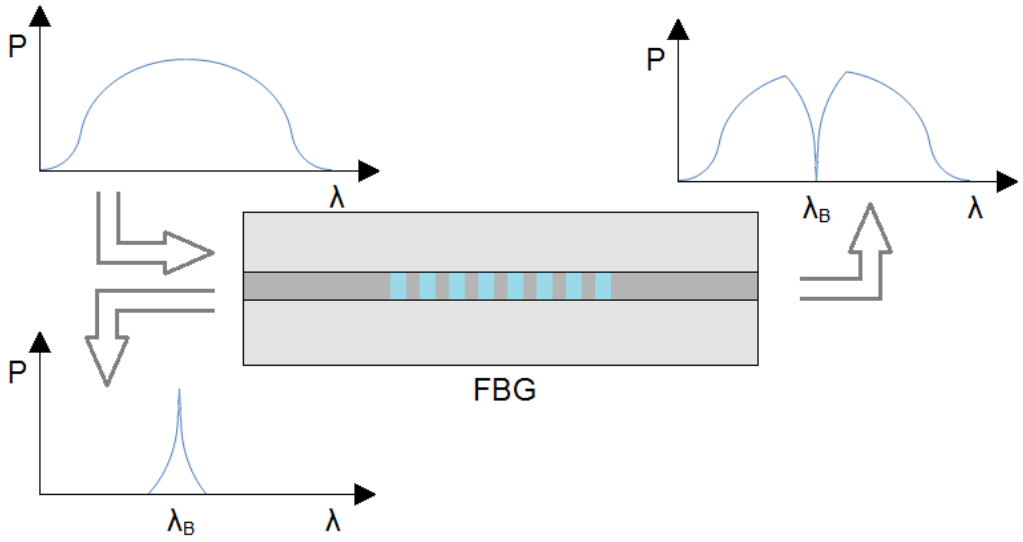

Figure 4.2 – Spectral response of a FBG. When light with a broad spectrum is launched into the fibre, the sensor will act as a filter reflecting a specific λ B wavelength and transmitting the other wavelengths.

Although straightforward, equation 4.1 does not explicitly show all the dependences that λ_B has with other parameters. FBGs are very versatile sensors in the sense that virtually any parameter that can cause the grating to elongate will be sensed. However, the core's effective index n_{eff} is also prone to fluctuate as a function of other perturbations. Indeed, FBGs have a rather complex dependence with strain and temperature, and the decoupling of these two when measuring poses some not so

trivial problems to solve. This relationship with strain and temperature is described by [44]:

$$\Delta n_{eff,x} = -\frac{n_{eff}^3}{2}\left[p_{11}\varepsilon_x + p_{12}(\varepsilon_y + \varepsilon_z)\right] + \frac{dn_{eff}}{dT}\Delta T \qquad (4.2)$$

$$\Delta n_{eff,y} = -\frac{n_{eff}^3}{2}\left[p_{11}\varepsilon_y + p_{12}(\varepsilon_x + \varepsilon_z)\right] + \frac{dn_{eff}}{dT}\Delta T, \qquad (4.3)$$

where p_{11} and p_{12} are the strain-optic coefficients, $\varepsilon_i (i = x, y, z)$ represents the mechanical strains along the principal axes, $\frac{dn_{eff}}{dT}$ is the thermal-optic coefficient and ΔT is the sensed temperature variation. In order to simplify the model, one can safely assume constant changes of strain and temperature along the fibre (z-direction) and an isotropic distribution of the written grating in the optical fibre. If equal transverse strains are now applied, then the physical description along the x and y axes becomes similar and equations 4.2 and 4.3 degenerate into one. However, if transverse strains are unequal then birefringence is induced in the grating. Being birefringence the difference between the effective refractive indexes of the fibre along different axes, light will travel with different speeds along different axes likewise. Hence, the detected reflective spectrum will be broader compared to the free-state single peak when no strain is applied.

Since temperature and strain have an effect both on the grating's length and the core's effective refractive index, one can relate the spectral shift of the Bragg wavelength as follows:

$$\frac{\Delta\lambda_{b,i}}{\lambda_B} = \frac{\Delta\Lambda}{\Lambda} + \frac{\Delta n_{eff,i}}{n_{eff}} \qquad (4.4)$$

The goal now is to be able to distinguish the two sources of spectral shift separately and to understand the different contributions coming from temperature and strain. To start, the term $\frac{\Delta\Lambda}{\Lambda}$ regarding the physical length change of the grating can be rewritten plainly as $\frac{\Delta\Lambda}{\Lambda} = \varepsilon_z + \alpha_f \Delta T$, namely as the sum of the longitudinal strain with the thermal strain, where α_f is the thermal expansion coefficient of the fibre. At the same time, some assumptions relating to strain measurements can be made that allows to simplify matters. Firstly, it is reasonable to take as a premise that the optical axes are aligned with the principal strain directions, given that birefringence is induced according to these last ones. Secondly, it is very common in embedded fibres that ε_x

and ε_y are sensibly equal, thus removing the birefringence phenomenon. Furthermore, longitudinal strain is often very large compared to transverse strain and can be described through the Poisson's ratio $\varepsilon_x = \varepsilon_y = -v_f \varepsilon_z$. Replacing in equation 4.4 one gets:

$$\frac{\Delta\lambda_b}{\lambda_B} = \varepsilon_z + \alpha_f \Delta T - \frac{n_{eff}^2}{2}\left[-p_{11} v_f \varepsilon_z + p_{12}(-v_f \varepsilon_z + \varepsilon_z)\right] + \frac{dn_{eff}}{dT}\Delta T \quad (4.5)$$

$$\frac{\Delta\lambda_b}{\lambda_B} = (1 - p_e)\varepsilon_z + K_T \Delta T \quad (4.6)$$

where $p_e = \frac{n_{eff}^2}{2}\left[(1 - v_f)p_{12} - v_f p_{11}\right]$ is called the effective optomechanical constant, v_f is the Poisson's ratio of the optical fibre and $K_T = \alpha_f + \frac{1}{n_{eff}}\frac{dn_{eff}}{dT}$ is a thermal constant that can be obtained experimentally after calibrating the sensors in their free state prior to their embedding. Equation 4.6 now shows a concrete dependence between strain, temperature and the reflected wavelength, but it is not clear how one should proceed if the aim is to understand the different influences of strain and temperature. Usually when measurements are taken to withdraw conclusions from one of the parameters, the other one is kept constant and vice-versa. But when both are free to change, the general solution frequently employed is to use a second sensor as a reference.

4.2 FBG sensing head

This section reports the implementation of a FBG laser sensor as acoustic sensor and studies its suitability for integration. Characterization has been carried out with the aid of a piezoelectric and a feedback system providing coherent light in a broad bandwidth. The method employed resembles the one used with Fabry-Pérot and allows for comparisons regarding sensitivity and range of detection.

4.2.1 Experimental setup

The FBG employed in the experiment was written in single mode optical fibre with femtosecond direct laser writing. This method allows for a point-by-point writing and uses a high-power source. After being written the first time, the grating was

rewritten but now with a very slightly different period – creating phase-shifted Moiré gratings. Such technique requires care due to the need of precise focusing and alignment, but has the upside of conferring the gratings very high reflectivity and habilitates their application in high temperature environments.

Acoustic characterization called for a system that would illuminate the grating and subsequently acquire the signal after it had sensed the acoustic wave. For that end an Erbium-doped fibre amplifier (EDFA) was used as a broadband source to supply the specific wavelength supported by the FBG. Seeing that the FBG operates in reflection mode, an optical circulator was inserted to link the FBG to the system. After connecting the output signal from the circulator back into the EDFA the feedback system was completed (Figure 4.3). This setup enabled the reflected Bragg wavelength to be greatly amplified and sensed distinctively from noise level. By coupling an optical spectrum analyser (OSA) to the setup one could then monitor the reflected Bragg wavelength and study how it behaved when the FBG was under an exterior perturbation.

A PZT was used as an acoustic source, much like in the way it was employed in the study of the Fabry-Pérot cavities. After fixing the FBG with tape to the optical table, the PZT was immobilized carefully on top of it. Added weights helped to ensure that the PZT was in physical contact with the FBG and that the conditions were sensibly the same in all the upcoming experiments. Supplying the PZT was a Stanford DS345 30 MHz function generator.

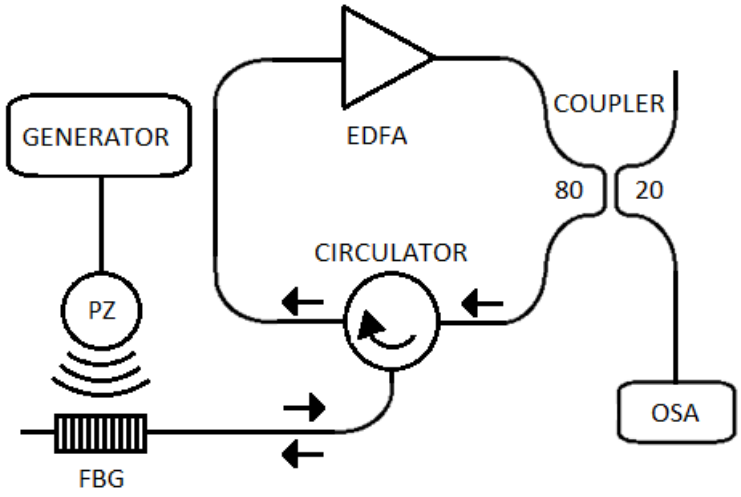

Figure 4.3 – Experimental setup for preliminary acoustic sensing and testing with FBGs. The OSA allowed real-time monitoring of the reflected peak Bragg wavelength and study of the lasing threshold current. Noticeable is the fact that since the sensing head works in reflection mode it is not deeply immersed within the setup, making it an easily embeddable element in other measurand structures.

After some preliminary testing with this setup, one concluded that the OSAs available at the lab did not qualify for precise measurements since they presented a small resolution relative to what was required and were not particularly user friendly when it came to data saving. Spectrums obtained with the configuration of Figure 4.3 showed clearly the laser's peak emission, but failed to provide meaningful data about the Bragg wavelength shift (Figure 4.4).

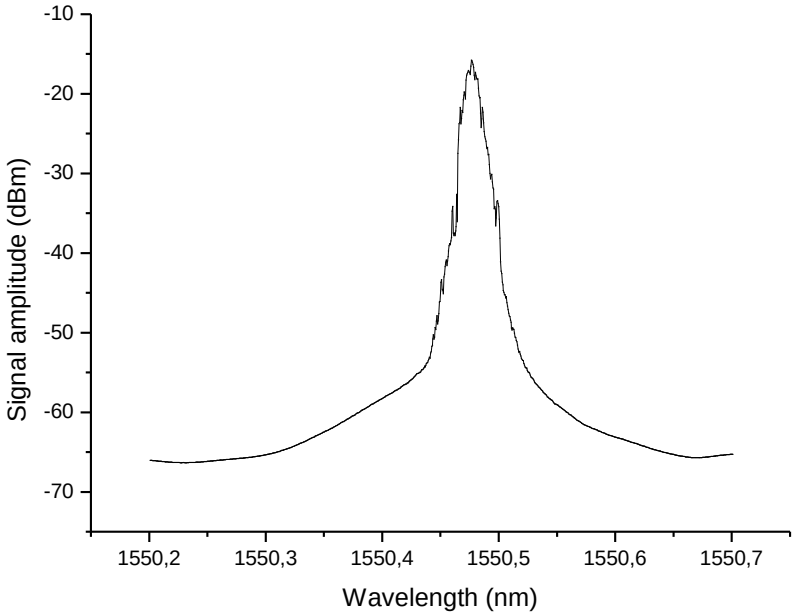

Figure 4.4 – Peak laser emission collected at the OSA with an applied PZT frequency of 1 kHz

Hence a new setup was adopted by replacing the OSA with an interrogation system composed by a wavelength-division multiplexer (WDM) filter, followed by a photodetector connected to an electronic spectrum analyser (ESA) preinstalled on a computer, the same PCI-5122 that was used when studying the Fabry-Pérot interferometers (Figure 4.5).

Beam splitting in the coupler ensured that a portion of light would pass on to a WDM. The role of this device was to act as a reference to the forthcoming acoustic characterization of the FBG laser sensor, providing a graphical relationship between the output intensity and the wavelength of operation. This was a key step for a meaningful interpretation of the intensity changes as wavelength variations, i.e. strains acting on the FBG. Subsequently the light beam reached a photodetector, where light was then guided through a coaxial cable with BNC connectors until it was collected by an ESA board. This spectrum analyser was controlled by a LabView program whose purpose was to return the frequency response of the system. The restrictions on the available frequency range for data sampling were the same as in the Fabry-Pérot case, namely the imposition to use frequencies below 60 kHz due to limitations of the PZT.

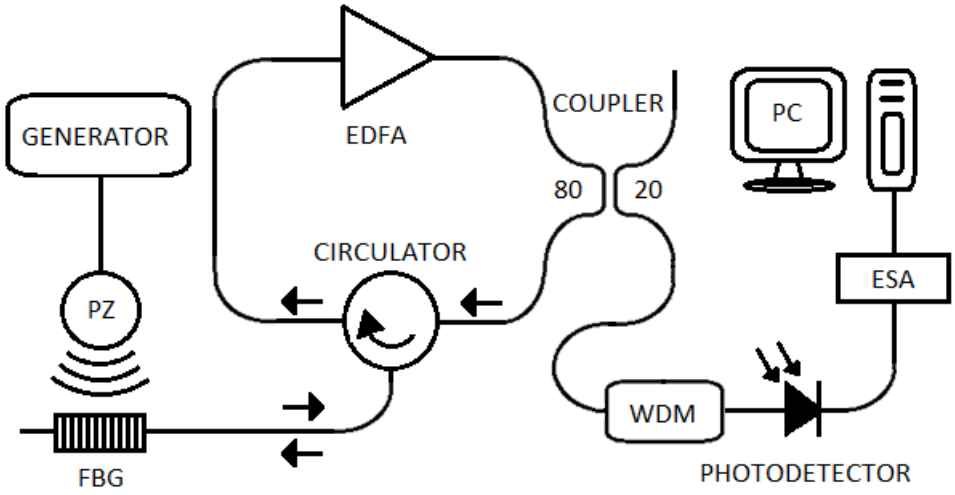

Figure 4.5 – Experimental design for acoustic sensing with FBGs. Substitution of the OSA for a more sensitive ESA system granted more resolution and data acquisition speed.

Acoustic characterization consisted mainly in collecting spectrums of the FBG laser sensor with different initial constraints set in the LabView program. These included range of detection, resolution, time of acquisition or averaging. Displacing the FBG and the PZT in slightly different positions in order to vary the contact surface between the two resulted in different spectrums as well.

Care was taken to allow sensible devices like the generator, the EDFA or the photodetector to stabilize for some time before the experiments, typically around 2 hours.

4.2.2 Results

In the previous chapter a study about the correct functioning of the lasing status of the system was done in order to assure reliability in the then upcoming results with Fabry-Pérot interferometers. The work developed with FBGs also asked for a study of the same kind, so as to guarantee that the operating laser would act correctly when sampling data. Peak amplitudes at the Bragg's wavelength $\lambda_B = 1550{,}465\, nm$ were then retrieved as a function of the input current of the EDFA to study the relationship between them. The results seem to indicate a linear behaviour (Figure 4.6). The threshold level set at the EDFA to achieve lasing was detected around 28 mA and the experimental points were sampled in the range between 30 and 130 mA, with a step of 5 mA. While the chosen step was adequate, the initial points between 30 and 55 mA proved to be unstable and hard to sample and were thus removed.

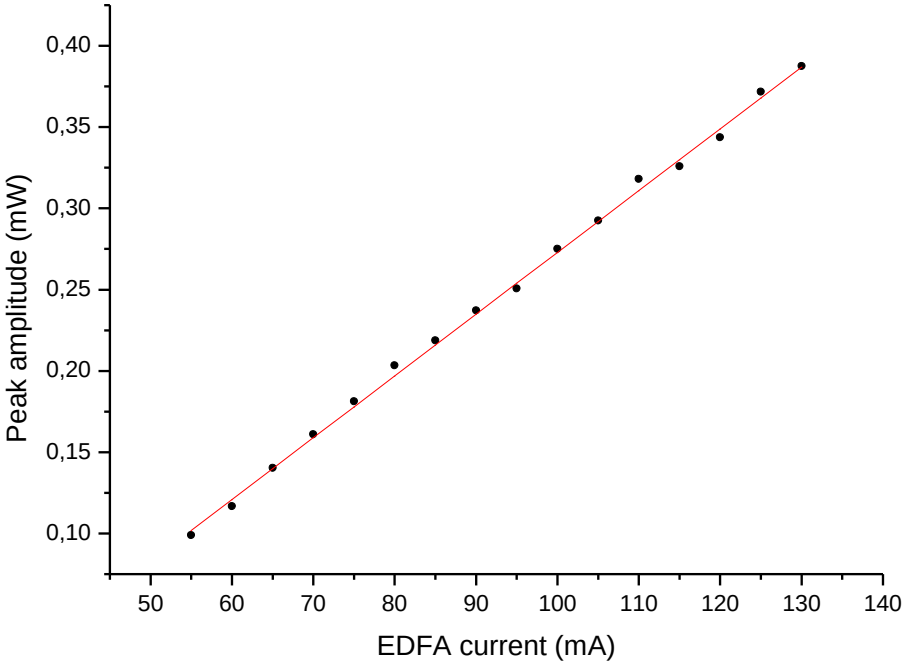

Figure 4.6 – Peak amplitudes at $\lambda = 1550{,}465$ sensed by an OSA as a function of the EDFA input current. The red fitting line indicates the expected linear behaviour.

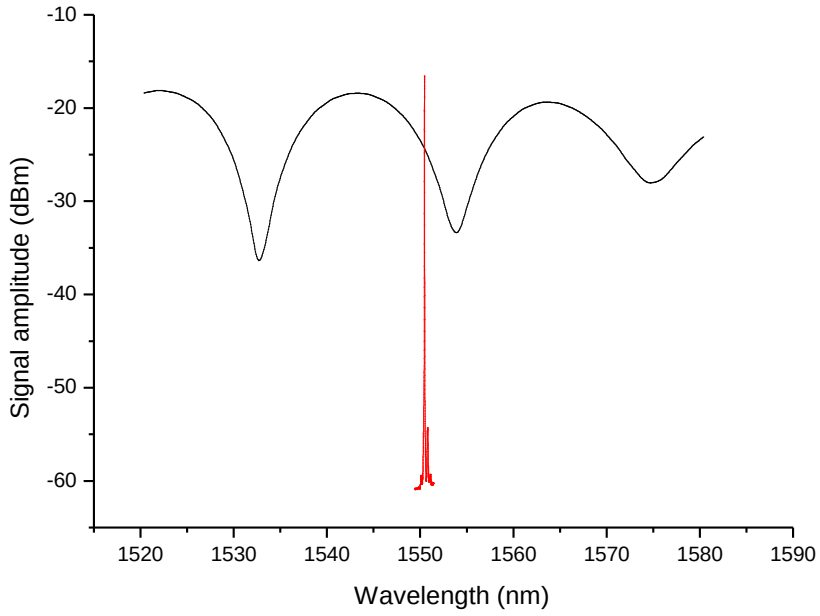

Figure 4.7 – Characteristic spectrum from a WDM (black line) used as a filter to sense Bragg wavelength shifts through changes in the received amplitude. Data was acquired by illuminating the FBG with a broadband light source and collecting the light beam in an OSA. Also present is the laser emission at the Bragg wavelength.

The first tries in sensing Bragg wavelength shifts due to neighbouring waves carrying specific frequencies were unsuccessful. The scheme adopted as in Figure 4.3

only revealed residual changes in the sensed peak wavelength in the OSA display. During this test the maximum $\Delta\lambda$ detected was 0,02 nm around the central peak emission wavelength although several parameters were tested and modified. This noise-like order of magnitude led to the conclusion that the $\Delta\lambda$ was small compared to the available OSA resolution and that an indirect measuring method should be preferred over the direct use of the OSA. Hence a WDM filter was introduced in order to establish a relationship between the detected intensity and the wavelength of the incoming light wave through the WDM's characteristic spectrum (Figure 4.7). The fact that the system's laser emits at a steep region of the WDM spectrum near the quadrature point is very important, since this feature adds sensitivity to the system. In this way any small change in the Bragg wavelength should be more easily spotted in the spectrum.

In order to study the acoustic response of the FBG, small step frequency sweeps were undertaken and the peak amplitudes for each set of data were retrieved. In this way, a profile of the device's sensitivity could be drawn, similarly to what was done previously with the Fabry-Pérot interferometers. Single frequency spectrums show that the sensed signal peaks are highly distinguishable from background noise (Figure 4.8). The acoustic characterization of the FBG laser sensor shows spectrums with high-frequency stable regions of operation having SNRs of 17 dB and 19 dB (Figure 4.9).

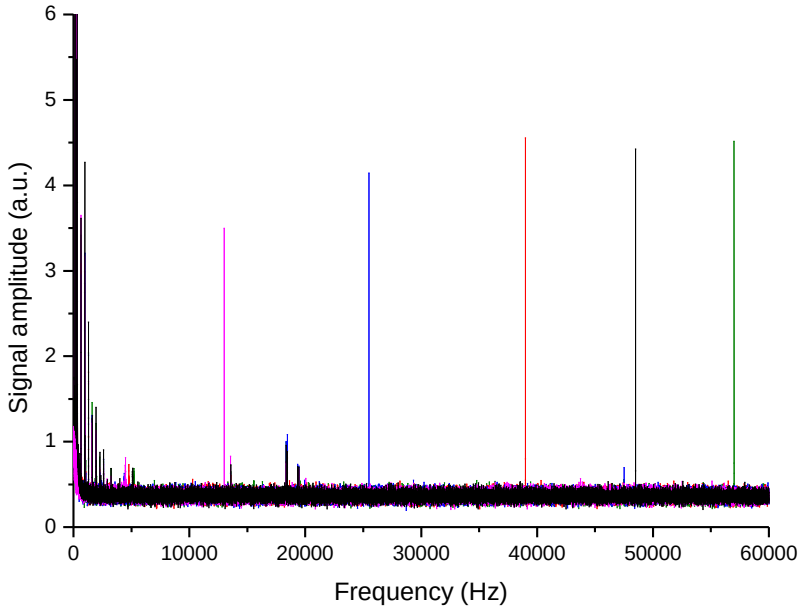

Figure 4.8 – FBG sensor frequency response to several exterior perturbations by the PZT.

Two sets of data were collected with the same initial conditions but with the exception that the position of the PZT on top of the grating was slightly changed. This shifted the amplitude and decreased sensitivity, but the overall behaviour was

maintained. Sharp peaks around 18 kHz and 20 kHz are due to external resonances as it can be seen in Figure 4.8.

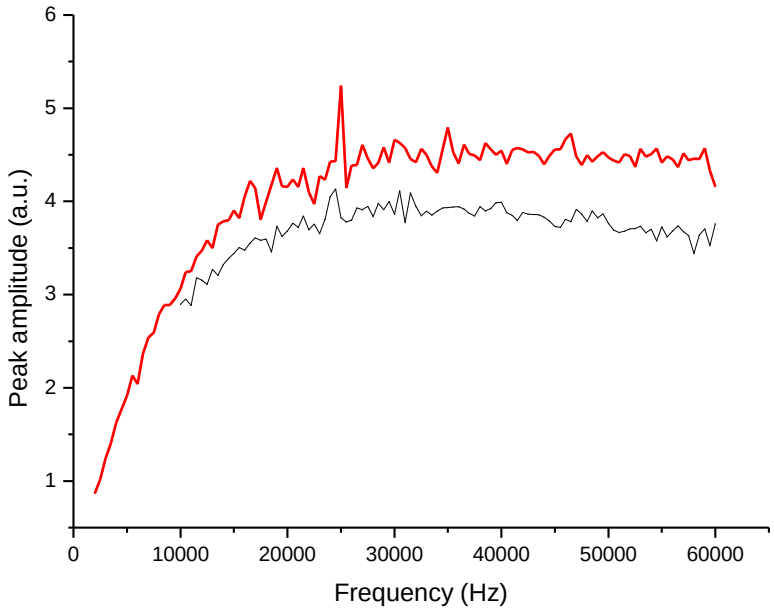

Figure 4.9 – Peak amplitude spectrums for two different frequency sweeps with the FBG acquired consecutively. The piezoelectric element was adjusted in slightly different positions on top of the grating to produce the two separate spectrums. *Red spectrum:* SNR = 19 dB; *black spectrum*: SNR = 17 dB.

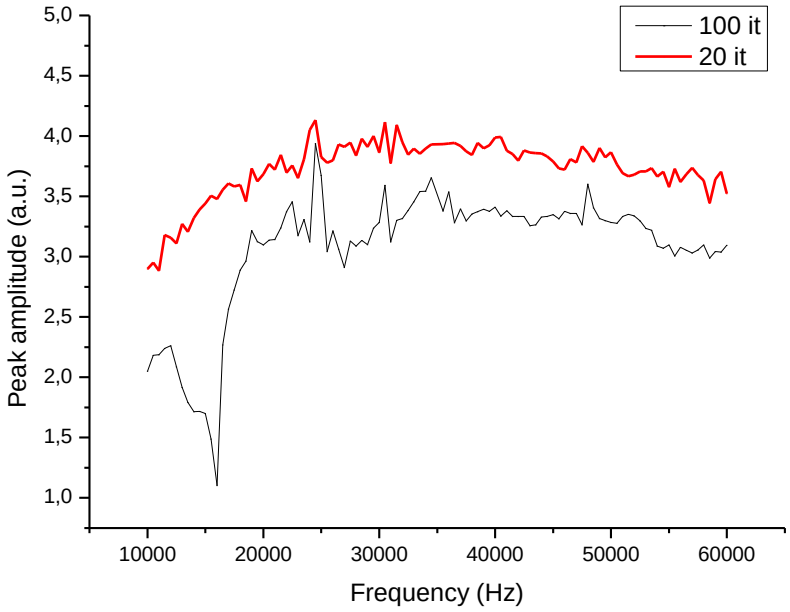

Figure 4.10 – Spectrums for the FBG sensor taken with 20 and 100 iterations. Noticeable is the effect this parameter has on averaging and on the final data display, influencing sensitivity and stability.

An important parameter when sampling was the correct adjustment of the number of wanted iterations for each set of data, as it had a direct impact both on the quality of the averaging process and acquisition time. Quick tests revealed no relevant differences between spectrums acquired when applying 20, 30 or 100 iterations. Still, a

full sweep was done for 20 and 100 iterations in order to study the effect of this parameter (Figure 4.10).

4.2.3 Discussion

The acoustic spectrum reveals that the FBG laser sensor is capable of high-frequency detection in the range between 0-60 kHz with a SNR over 17 dB. At low frequencies the detected signals suffer from high instability and the presence of $1/f$ noise, but at higher frequencies the time response remains constant. This means that the intensity changes in the range between 10-60 kHz are caused by modulation of the WDM through shifts in the Bragg wavelength. The system can hence be applied for the detection of high-frequency bursts, typically acoustic crack emissions generated by aging processes in concrete structures. In this frame of thought, an interrogation system encompassing three FBG laser sensors could be used to spatially localize cracks in a material through a triangulation process.

4.3 FBGs in 3D woven composites

As part of a one-month summer internship supported by the University of Manchester, this subchapter reports the work developed at the Aerospace Research Institute in Manchester, United Kingdom. The goal was to embed OFSs in 3D woven composites and attempt a verification of strain distributions along the composite. After a short introduction to the field of composites, the experimental procedure for the sample preparation is described, followed by results for the infusion process monitoring.

4.3.1 Introduction to composites

When two or more materials are combined to form another material with properties not seen in any of the original constituents, one obtains a composite. It consists of a bulk material that acts as the main structure (the matrix) and a reinforcing material that adds stiffness, usually in fibre form. The right combination of matrixes and fibres can produce exceptionally strong composites, leading to applications in aerospace parts where often it is required for materials to overcome environments with

extreme conditions [45]. Carbon, glass and aramid are among the most common fibre materials, while polyester and epoxies are the most used as matrixes.

With the advent of material fabrication in fibre form, it has been discovered that some apparently fragile materials in bulk (such as glass) can be transformed into a very strong fibre form. In bulk form, applied stresses produce cracks that propagate and deteriorate the whole material rapidly due to random surface defects; however, in fibre form, the cracks will only affect a discrete number of fibres, leaving the rest of the material intact. In this way, the theoretical strength of the materials is best seen when in fibre form.

Although strong, fibres have preferential directions in which they show their best properties, namely along its length. The ideal case of having a material that would present great isotropic mechanical properties started to be solved when resins were used to glue the fibres together. While resins do not have extraordinary mechanical properties on their own, they do have the ability to be easily shaped into different forms. Allying the tensile strength of the fibres with the homogeneity of applied stress distribution provided by the resin matrix creates light materials with superb mechanical properties, outperforming the industry-based metals in many aspects and possible applications. What is more interesting and promising about these composites though, is the fact that the set of final properties depends not only on the previous properties of the matrix and the reinforcing material, but depends also on the fabrication process. This is something not found when working with metals, for example, where the material's specifications are given by the supplier.

When building a composite, fibres are weaved together forming fabrics in order to attain the best mechanical properties. Traditionally, through processes of interlocking these well determined patterns produce 2D layer sheets of fibres that can eventually be stacked together to form thicker fabrics. By adding a matrix, 2D composites are then formed, revealing notable in-plane properties, but suffering however from delamination problems because of their sheet structure. This setback is translated into poor performance when strains and stresses from impact loads are applied in specific directions, causing the material to fail. To circumvent these problems 3D composites were developed integrating complex structures of orthogonally interlocked fibres, conferring isotropic mechanical properties [46]. The several available techniques (such as 3D weaving, 3D braiding or 3D stitching) all require specialised and expensive instrumentation which thus confines 3D composites usage to highly engineered applications.

Currently there are several fabric types that can be achieved by interlacing warps (longitudinal threads) and wefts (transverse threads), with different configurations displaying different levels of fibre crimp, difficulty in draping and stability (Figure 4.11). Plain, twill and leno (with variants) are the most commonly seen woven fabrics configurations.

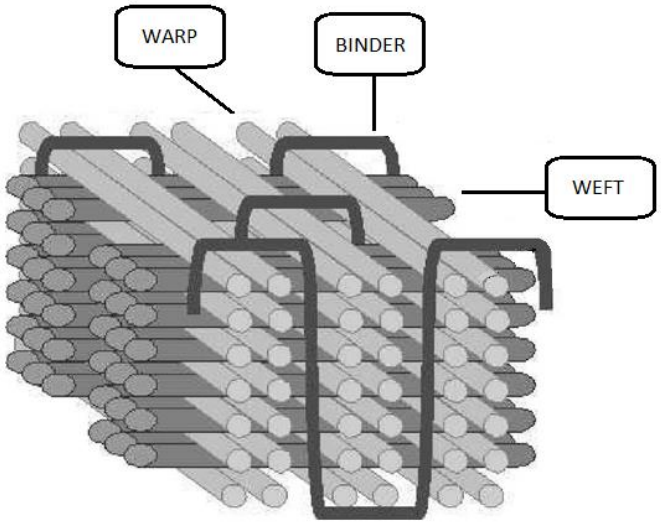

Figure 4.11 - General structure of a 3D woven composite (adapted from [47])

The process of joining the fabric with the polymer based resin is generally a complex process, with the main objective being a homogeneous spread of the resin along the fabric. Several different infusion methods have been developed; from the simple spray or hand lay-up processes to the more sophisticated resin transfer moulding, each technique is more suited to a specific set of fibres and resins. Adding to this are constraints regarding both safety and environmental hazards imposed by the toxic nature of the resins.

After spreading the resin through the fabric, the mixture needs to undergo a curing process where the resin reacts chemically to form a thermoset structure, achieving its best mechanical properties at the gel point. It is therefore common for the resin to be supplied together with a suitable hardener in the correct proportion, since this parameter weighs heavily in the final properties. Most resins require heat for the curing process to be held with the reaction rate doubling with each 10 ºC increase, approximately and curing temperatures range typically from 50-150 °C. Heating is made in a step-by-step basis, with slow increases in order to keep the highly exothermic reaction under control and to not allow the heat to build up locally in the sample.

4.3.2 Experimental method

Key to the assessment of the final structure's performance is the composite's response to applied stresses and strains. For this effect there are mechanical tests available, but to understand at a more fundamental level how the composite behaves it is most useful to study locally the strain response, in particular at the interstitial junctions between warps and wefts. FBGs sensors quickly turned out to be the main choice as sensors since a fully automatized interrogation system for FBGs was available. In the other hand, the also available Fabry-Pérot sensors required other optical devices that would make the measurements much more difficult.

The fabric used was a 2x2 twill angle interlocked (11 picks/cm) woven fabric made of glass fibre with dimensions 14 x 7,5 cm. The FBG was placed in the centre of the fabric to avoid boundary effects; its embedment in an interstitial zone between one warp and one weft was achieved with the aid of a needle and required great care due to the tightness of the fabric and the brittle nature of the FBG sensor. The chosen matrix was a hot curing epoxy system with Araldite® LY564, a low-viscosity epoxy resin, and Aradur® 2954, a cycloaliphatic polyamine acting as an epoxy hardener. This system combines long pot life and low viscosity with excellent post-cure mechanical properties, being particularly suitable for aerospace applications.

Figure 4.12 - Twill angle interlock glass fibre woven fabric with the FBG inserted between a warp and a weft.

A wet lay-up method with vacuum bagging was carried for the infusion process. The fabric was laid on a steel plate and covered with peel ply to enhance the homogeneity of the finished surface after curing. A tacky-tape was placed alongside all the borders to prevent vacuum failure with extra attention to the zone containing the output fibre from the FBG sensor and vacuum pipes. After successfully sealing the system with a vacuum bag, the setup was ready to proceed to the infusion of the resin (Figure 4.13).

A vacuum pump system was connected to the setup so as to control the rate flow of the resin inside the bag. Slow rates were preferred over fast rates since it improved the chances of the resin fulfilling every cavity and gap along and between the glass fibres. Ideally the resin would be in close contact with the fibres not allowing air bubbles to settle and being a source of material failures.

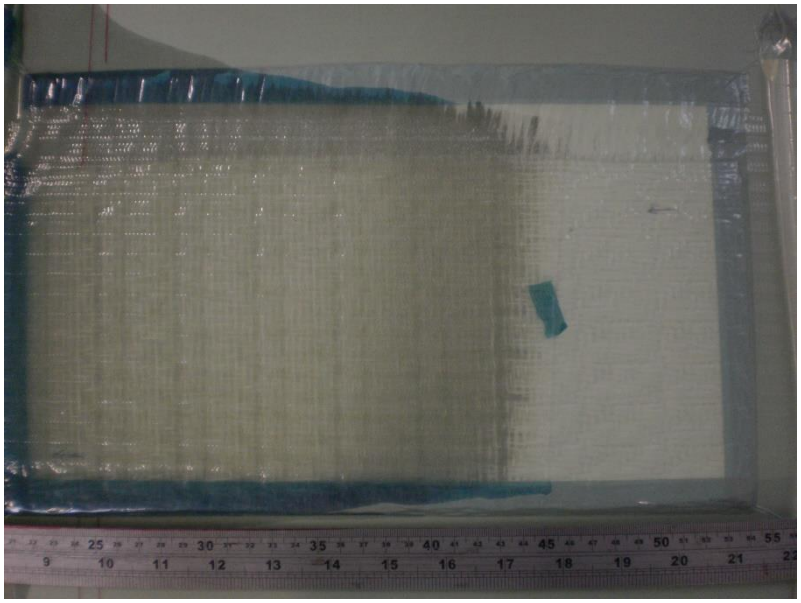

Figure 4.13 – Infusion process with resin approaching the FBG sensor.

A study of the sensor response to strains during the infusion was achieved through monitoring of the reflected Bragg wavelength. For this effect, a MicronOptics sm125 FBG interrogator was connected to the FBG, displaying real time shifts of the Bragg wavelength in a ready-to-use interface. It worked by sending broadband light into the fibre and analysing the reflected wavelengths in the same channel.

After the infusion process the sample plate was taken to an oven where the curing took place. In accordance with the supplier's guidelines the curing cycle took 4 hours at 60ºC followed by 8 hours at 120ºC and then 4 hours until decreasing to ambient temperature.

4.3.3 Results

The monitoring of the infusion process shows the grating being mainly compressed as the resin spread around the fabric and induced strains (Figure 5.1). This indicates that distributing sensing in the fabric could be a good approach to achieve validation of a computational model for strain distribution. Pre-infusion tests already revealed high sensitivity from the FBG sensing head, with direct physical tapping resulting in shifts of Bragg wavelength in the order of 10^{-1} nm. Prior to the vacuum pumping the sensor was stable with a Bragg wavelength of 1550,4 nm, but after the vacuum had been established the grating underwent elongation. Then, as the resin started to be infused, the pressure inside the vacuum bag increased and caused the grating to enter a state of relaxation, shrinking towards its original length. This is quite possibly the reason because there is a linear decrease of the reflected Bragg wavelength, sensibly during the first 12,5 minutes after the beginning of the infusion process. As for the steep decrease between 12,5 and 18 minutes, it is caused by strains prompted by the resin thermosetting around the fabric. It is interesting to note that since the FBG was placed in a central zone of the fabric the resin did not immediately came into contact with the FBG; however, this did not hindered the strains

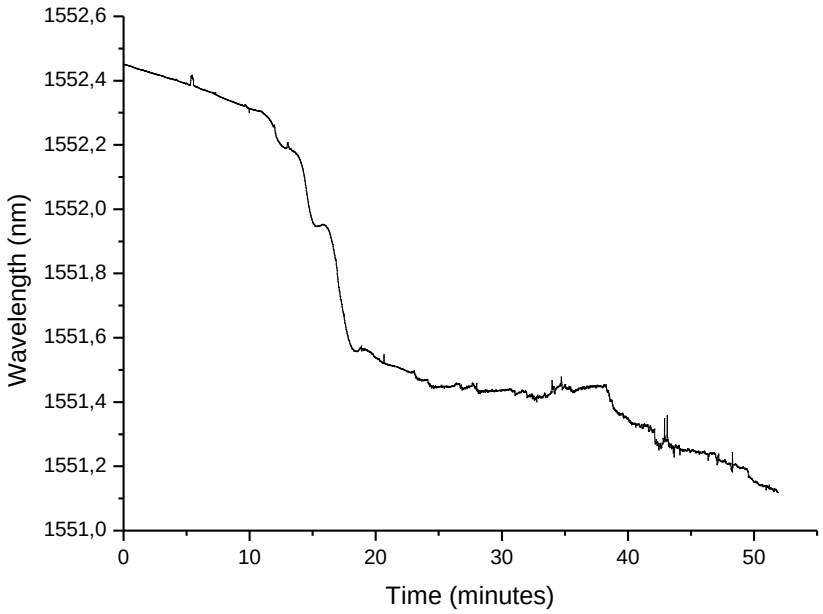

Figure 4.14 - Profile of the reflected Bragg wavelength during the infusion process.

caused by the resin away from the grating to also be sensed. Indeed, the resin only reached physically the FBG after 13 minutes. At 24 minutes the Bragg wavelength

showed signs of stabilization; surely around this point the resin had already covered the entire fabric, although it still continued to flow inside of the bag. After 34 and 43 minutes adjustments with the equipment positioning needed to be done and contact with the supporting table was unavoidable. These gestures were readily sensed as peaks and oscillations.

4.3.4 Discussion

The FBG sensing scheme proved to be an effective device for monitoring infusion processes, and can be used for mapping strain distribution. Monitoring during the curing cycles and vacuum pumping can also provide a clearer view on the spectrum response of the sensor. Proper encapsulation and protection of both the FBG and the linking optical fibre are critical aspects to be developed if this monitoring method is to become economically feasible.

5 Conclusions and future work

Chapter two saw an introduction to optical sensors and their features as acoustic sensors. A literature review was done, highlighting mainly the important developments in Fabry-Pérot interferometry and fibre Bragg gratings.

In chapter three the focus was on in-line designs of Fabry-Pérot sensors. The development of several sensing heads and acoustic characterization led to the conclusion that they are mostly suitable for micro-applications, where small size and embedding capabilities are a must. High sensitivity coupled with flexibility and resistance to moisture and other chemicals make these sensors a viable alternative to the majority of electrical gauge technologies.

Fibre Bragg gratings were examined in chapter four. Although there was no success in retrieving the reflected Bragg wavelengths, results showed very good sensitivity and ability to detect single frequencies amidst the background noise. According to the experiments FBGs are prone to have success in fields that require sensing of faint signals and strains.

Smart structures involving optical fibre sensors and composite structures (such as polymers or carbon fibre structures) are likely to become a busy topic of research since the demanding industry that produces the applications of these structures also is in need of a reliable method of monitoring their performance. More specifically, future work connected to Fabry-Pérot interferometry and optical fibre sensing should see developments regarding:

- A fast and concise way of producing FP sensing heads in the submicron range, abandoning the purely mechanical methods;
- Higher splice quality, which would lead to a greater reflectivity and subsequently to an increase in sensitivity;
- The use of pencil lead breaks as a cheap way of characterizing the acoustic response of the sensor;
- Applications in harsh chemical environments where FPs outperform the existent electric gauges;

In its turn, FBGs should experience developments in:

- Improved embedding processes, with adequate coatings that do not interfere with the sensing scheme as well as introduced unwanted strains on the grating.
- Higher reliability in temperature and strain simultaneous measurements.

- Assessment of the safety and integrity of engineering structures through the exploration of its multiplexing abilities. This area should push the development of FBGs forward in order to meet the demands of the nowadays strict safety restrictions.

Still, and in spite of its promising results and applications, fibre optic systems are currently too expensive for massive commercialization and general public use. New strategies towards lowering costs are expected as improvements in technological advances keep probing the scientific community for improved sensing devices.

Annex

Present in this annex is the impedance response of the PZT used throughout the development of this thesis. After gaining knowledge about this feature it was possible to choose more wisely the frequency ranges with which the acoustic characterization was possible, without having PZT resonances disturbing the spectrum.

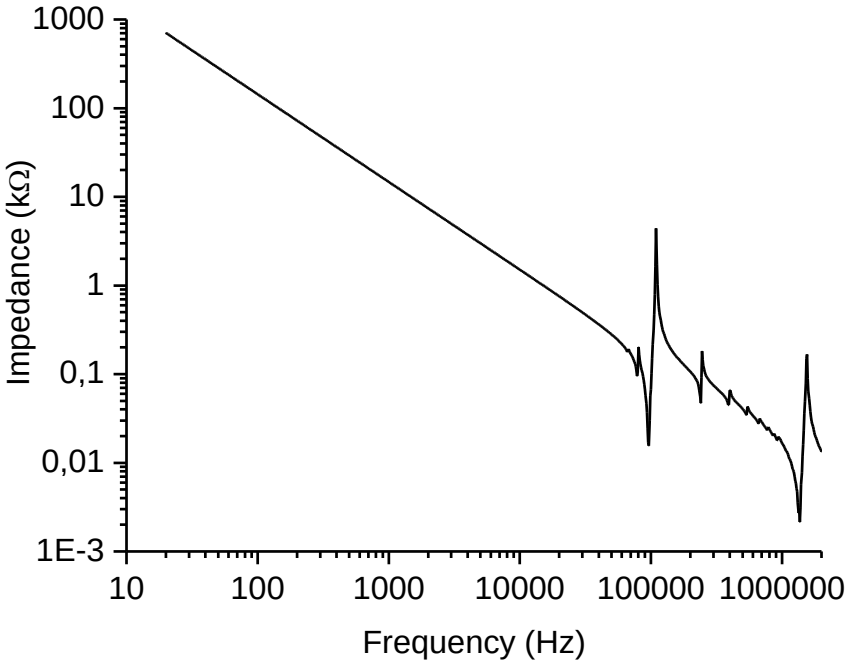

Figure 5.5.1 – Impedance response of the piezoelectric.

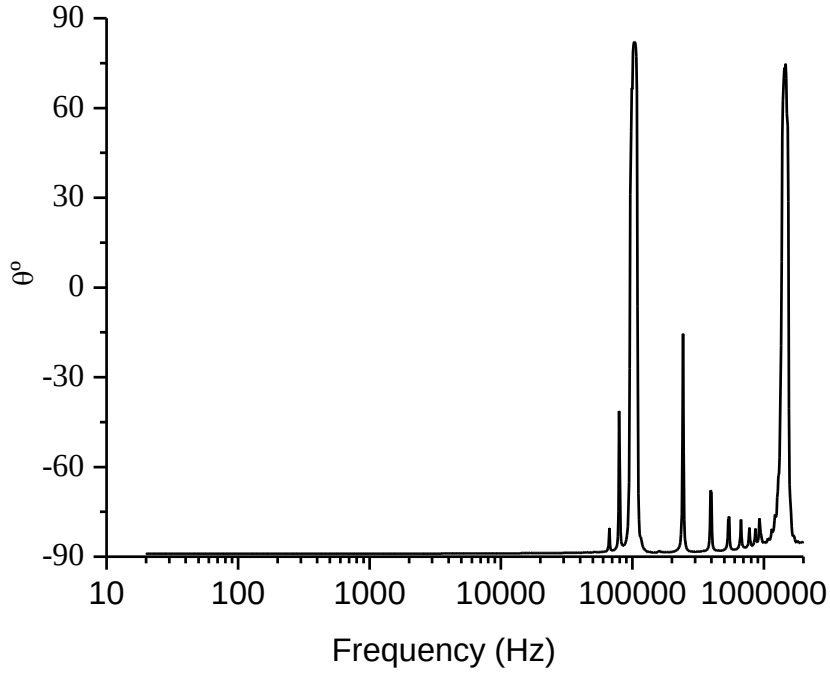

Figure 5.5.2 – Angular response of the piezoelectric.

References

1 Byeong Ha Lee, Young Ho Kim, Kwan Seob Park, Joo Beom Eom, Myoung Jin Kim, Byung Sup Rho, and Hae Young Choi, "Interferometric fiber optic sensors," Sensors **12** (3), 2467-2486 (2012).

2 G Wild and S Hinckley, "Acousto-ultrasonic optical fiber sensors: overview and state-of-the-art," IEEE Sensors Journal **8** (7), 1184-1193 (2008).

3 Y Geng, X Li, X Tan, Y Deng, and X Hong, "Compact and ultrasensitive temperature sensor with a fully liquid-filled photonic crystal fiber Mach-Zehnder interferometer," IEEE Sensors Journal **14** (1), 167-170 (2014).

4 PM Junghare, S Kulkarni, and R Mulimani, "Mach-Zehnder Interferometer Sensor for Acoustic Detection with Optimal Performance," Journal of Electronics and Communication Engineering **2** (5), 29-33 (2012).

5 JA Bucaro, HD Dardy, and EF Carome, "Optical fiber acoustic sensor," Applied Optics **16** (7), 1761-1762 (1977).

6 TK Lim, Y Zhou, Y Lin, YM Yip, and YL Lam, "Fiber optic acoustic hydrophone with double Mach–Zehnder interferometers for optical path length compensation," Optics Communications **159** (4), 301-308 (1999).

7 PM Junghare, CP Raj P, T Srinivas, and P Sharan, "A Finite Element Analysis of Fiber Optic Acoustic Sensing Mandrel for Acoustic pressure with Increased Sensitivity," American Journal of Engineering Research **2** (9), 1-7 (2013).

8 N Chen, Y Hsieh, and Y Lee, "Tapered fiber Mach-Zehnder interferometers for vibration and elasticity sensing applications," Optics Express **21** (9), 11209-11214 (2013).

9 N Lagakos, P Ehrenfeuchter, TR Hickman, A Tveten, and JA Bucaro, "Planar flexible fiber-optic interferometric acoustic sensor," Optics Letters **13** (9), 788-790 (1988).

10 AI Hernández-Serrano, G Salceda-Delgado, D Moreno-Hernández, A Martínez-Ríos, and D Monzón-Hernández, "Robust optical fiber bending sensor to measure frequency of vibration," Optics and Lasers in Engineering **51** (9), 1102-1105 (2013).

11 G Paltauf, R Nuster, M Haltmeier, and P Burgholzer, "Photoacoustic tomography using a Mach-Zehnder interferometer as an acoustic line detector," Applied optics **46** (16), 3352-3358 (2007).

12 M Imai, T Ohashi, and Y Ohtsuka, "High-sensitive all-fiber Michelson interferometer by use of differential output configuration," Optics Communications **39** (1), 7-10 (1981).

13 X Hong, J Wu, C Zuo, F Liu, H Guo, and K Xu, "Dual Michelson interferometers for distributed vibration detection," Applied optics **50** (22), 4333-4338 (2011).

14 RW Speirs and AI Bishop, "Photoacoustic tomography using a Michelson interferometer with quadrature phase detection," Applied Physics Letters **103** (5), 053501-053501-053505 (2013).

15 E Udd, presented at the Single Mode Optical Fibers, San Diego, California, 1983 (unpublished).

16 BJ Vakoc, MJF Digonnet, and GS Kino, "A novel fiber-optic sensor array based on the Sagnac interferometer," Journal of Lightwave Technology **17** (11), 2316-2326 (1999).

17 TS Jang, SS Lee, and YG Kim, "Surface-bonded fiber optic Sagnac sensors for ultrasound detection," Ultrasonics **42** (1), 837-841 (2004).

18 L Yuan, L Zhou, and W Jin, "Detection of acoustic emission in structure using Sagnac-like fiber-loop interferometer," Sensors and Actuators A: Physical **118** (1), 6-13 (2005).

19 J Zhang, J Wen, X Wang, S Jiao, and F Wang, "A Novel Leakage Detection Method for Long Distance Gas Pipelines Based on Optic Fiber Sensor and Optical Multiplexing," Bridges **10**, 601-608 (2014).

20 L Wang, N Fang, C Wu, H Qin, and Z Huang, "A Fiber Optic PD Sensor Using a Balanced Sagnac Interferometer and an EDFA-Based DOP Tunable Fiber Ring Laser," Sensors **14** (5), 8398-8422 (2014).

21 P Rohwetter, C Lothongkam, W Habel, G Heidmann, and D Pepper, presented at the 23rd International Conference on Optical Fiber Sensors, Santander, Spain, 2014 (unpublished).
22 KA Murphy, MF Gunther, AM Vengsarkar, and RO Claus, "Quadrature phase-shifted, extrinsic Fabry–Perot optical fiber sensors," Optics Letters **16** (4), 273-275 (1991).
23 Y Rao, "Recent progress in fiber-optic extrinsic Fabry–Perot interferometric sensors," Optical Fiber Technology **12** (3), 227-237 (2006).
24 P Morris, A Hurrell, A Shaw, E Zhang, and P Beard, "A Fabry–Pérot fiber-optic ultrasonic hydrophone for the simultaneous measurement of temperature and acoustic pressure," The Journal of the Acoustical Society of America **125** (6), 3611-3622 (2009).
25 K Kim, Y Mizuno, and K Nakamura, "Fiber-optic ultrasonic hydrophone using short Fabry–Perot cavity with multilayer reflectors deposited on small stub," Ultrasonics **54** (4), 1047-1051 (2014).
26 J Ma, H Xuan, HL Ho, W Jin, Y Yang, and S Fan, "Fiber-Optic Fabry–Pérot acoustic sensor with multilayer graphene diaphragm," IEEE Photonics Technology Letters **25** (10), 932-935 (2013).
27 LH Chen, CC Chan, W Yuan, SK Goh, and J Sun, "High performance chitosan diaphragm-based fiber-optic acoustic sensor," Sensors and Actuators A: Physical **163** (1), 42-47 (2010).
28 B Dong, M Han, and A Wang, presented at the Fiber Optic Sensors and Applications IX, Baltimore, Maryland, USA, 2012 (unpublished).
29 Kun Wang, Xinglin Tong, and Xiaolong Zhu, "Transformer partial discharge monitoring based on optical fiber sensing," Photonic Sensors **4** (2), 137-141 (2014).
30 KO Hill, Y Fujii, DC Johnson, and BS Kawasaki, "Photosensitivity in optical fiber waveguides: Application to reflection filter fabrication," Applied Physics Letters **32** (10), 647-649 (1978).
31 Y Rao, "In-fibre Bragg grating sensors," Measurement science and technology **8** (4), 355-375 (1997).
32 DJ Webb, J Surowiec, M Sweeney, DA Jackson, LR Gavrilov, JW Hand, L Zhang, and I Bennion, presented at the Fiber Optic and Laser Sensors XIV, Denver, Colorado, 1996 (unpublished).
33 NE Fisher, J Surowiec, DJ Webb, DA Jackson, LR Gavrilov, JW Hand, L Zhang, and I Bennion, "In-fibre Bragg gratings for ultrasonic medical applications," Measurement science and technology **8** (10), 1050-1054 (1997).
34 HJ Kalinowski, I Abe, JA Simões, and A Ramos, "Application of fibre Bragg grating sensors in biomechanics ", in *Trends in Photonics* (Research Signpost, 2010).
35 A Acquafresca, E Biagi, L Masotti, and D Menichelli, "Toward virtual biopsy through an all fiber optic ultrasonic miniaturized transducer: a proposal," IEEE Transactions on Ultrasonics, Ferroelectrics and Frequency Control **50** (10), 1325-1335 (2003).
36 THT Chan, L Yu, H Tam, Y Ni, SY Liu, WH Chung, and LK Cheng, "Fiber Bragg grating sensors for structural health monitoring of Tsing Ma bridge: Background and experimental observation," Engineering structures **28** (5), 648-659 (2006).
37 Y Qiu, Q Wang, H Zhao, J Chen, and Y Wang, presented at the Symposium on Photonics and Optoelectronics (SOPO), Shanghai, 2012 (unpublished).
38 MA Davis, DG Bellemore, and AD Kersey, "Distributed fiber Bragg grating strain sensing in reinforced concrete structural components," Cement and concrete composites **19** (1), 45-57 (1997).
39 CU Grosse and M Ohtsu, *Acoustic emission testing: basics for research—applications in civil engineering*. (Springer, 2008).

40 A Minardo, A Cusano, R Bernini, L Zeni, and M Giordano, "Response of fiber Bragg gratings to longitudinal ultrasonic waves," IEEE Transactions on Ultrasonics, Ferroelectrics and Frequency Control **52** (2), 304-312 (2005).

41 Amir Rosenthal, Daniel Razansky, and Vasilis Ntziachristos, "High-sensitivity compact ultrasonic detector based on a pi-phase-shifted fiber Bragg grating," Optics letters **36** (10), 1833-1835 (2011).

42 H Tsuda, K Kumakura, and S Ogihara, "Ultrasonic sensitivity of strain-insensitive fiber Bragg grating sensors and evaluation of ultrasound-induced strain," Sensors **10** (12), 11248-11258 (2010).

43 Charles D Butter and GB Hocker, "Fiber optics strain gauge," Applied optics **17** (18), 2867-2869 (1978).

44 RJV Steenkiste and GS Springer, *Strain and temperature measurement with fiber optic sensors*. (Technomic Publishing Company Incorporated, 1996).

45 AP Mouritz, MK Bannister, PJ Falzon, and KH Leong, "Review of applications for advanced three-dimensional fibre textile composites," Composites Part A: applied science and manufacturing **30** (12), 1445-1461 (1999).

46 J Brandt, K Drechsler, and F-J Arendts, "Mechanical performance of composites based on various three-dimensional woven-fibre preforms," Composites Science and Technology **56** (3), 381-386 (1996).

47 S Rudov-Clark and AP Mouritz, "Tensile fatigue properties of a 3D orthogonal woven composite," Composites Part A: Applied Science and Manufacturing **39** (6), 1018-1024 (2008).